Universidad de los Andes

PHYSICS DEPARTMENT

MEASUREMENT AND CHARACTERIZATION OF GRANULATION PATTERN IN THE IAG SOLAR FLUX SPECTRUM

Second version

BSc Physics Final Project

Author:

Claudia Alejandra Cuellar Nieto

Advisor:

Benjamin Oostra Vannoppen

Nov 2025

Abstract

Hello, this is my work:D The present project analyses the three signatures of convection presentes on the solar spectrum. Measurement of the granulation pattern, Characterization of the wavelengthdependence on many feautres of the star clears the concept of convection in the Sun.

Acknowledgements

Thanks to miku and ado for the playlist to work, and Benja:D

Contents

List of Figures

5

Chapter 1

Introduction: The Sun's granulation pattern

For decades, the solar spectrum has served as the fundamental reference point for spectroscopic analysis. As our nearest star, the Sun enables detailed studies of stellar composition. However, advances in optical instrumentation have revealed previously undetected spectral details, providing new insights into fundamental solar properties One key insight is the granulation pattern caused by convective motion, which is characterized by three distinct hydrodynamic signatures: Line broadening, line profile asymmetry, and the line-depth dependence of convective blueshift.

Inspired by David Gray's foundational research ([9] and references therein), this project aims to extract the granulation pattern from the IAG Solar Flux Atlas to calculate relative velocities and perform a detailed analysis based on the three signatures of convection.

1.1 Convective motion

The stellar spectrum serves as astronomy's primary source of information, encoding details about a star's composition and velocity. However, in some stars this spectrum is modified by fluid motions caused by density variations from temperature fluctuations in the outermost layer, where each spectral line exhibit a distinct velocity shift. These persistent convective

motions generate a granular structure in the solar photosphere, a phenomenon supported by extensive research (see [10, 5, 9]).

The granulation in the Sun photosphere was first observed as a moving granular structure by Janssen in 1885. Later, in 1901, Plaskett associated this pattern with the convective cells observed in Bénard's experiment [4], where fluids heated from below produces rising elements of hot gas convecting heat to the surface. This characteristic configuration gives the name *granulation* to all observable signs of solar convection.

1.1.1 The three signatures of convection

Convective motion produces three signatures of granulation in stellar spectra: Line broadening, line profile asymmetry, and line-depth dependence of convective blueshift [11]. This project focuses on the third signature, which exhibits a correlation between line depth and relative velocity. The method for quantifying this relationship is known as the *granulation pattern*, which means the plot of relative velocities against line depth [9].

The physical origin of this pattern lies in the convective process itself. When the Sun pushes material up through its outer layer, the spectrum exhibits a blueshift. As this material subsequently cools and falls back through the atmosphere, it produces a redshift but emits less light, making the blueshift dominant. Neutral iron lines (Fe I) are optimal for calibrating this phenomenon due to their high abundance, minimal thermal broadening, limited isotopic variation and availability of accurate laboratory measurements of natural wavelengths. Furthermore, the even number of nucleons in the most abundant isotope resulting in no hyperfine structure shown. The use of a single chemical species offers the additional advantage of retrieving natural wavelengths from a single source, thereby eliminating potential discrepancies [12].

The study of granulation patterns has been significantly documented by David Gray, whose work has improved the precision of stellar radial velocity measurements ([9] and references therein). This improvement stems primarily from his observation that granulation patterns in solar-type stars closely resemble the solar pattern, differing primarily by a scaling factor. This is particularly significant given the considerable challenges of obtaining such precise measurements for other stars, which are often affected by spectral noise, stellar proper motions,

and velocity uncertainties [9]. Furthermore, analyzing solar granulation patterns is crucial for validating photospheric hydrodynamic models [5], enabling improved calibration and testing of dynamic atmospheric models.

Following the motivation of treating the Sun as any other star, which does not have the angular resolution necessary to study the spatial granulation structure, the most accurate solar flux atlas is necessary.

1.2   The IAG solar flux atlas

In 2016, Reiners and colaborators published the unprecedented precision *Institut für Astrophysik und Geophysik* (IAG) solar flux atlas obtained with the FTS *Fourier Transform Spectrograph* at Göttingen, simultaneously reporting convective blueshifts for a sample of Fe I lines. This atlas provides highly precise and accurate data, with radial velocity uncertainties on the order of ± 10 m/s across the wavelength range of $4050\,\text{Å}$ to $10\,650\,\text{Å}$. In contrast to other FTS atlases, the entire visible wavelength range was observed simultaneously using only one spectrograph setting [13].

Despite the exceptional quality of the spectrum, the first derived granulation pattern appeared notably scattered and noisy. This was attributable to a rudimentary line position measurement methodology and a poor line selection, which included numerous blended features, outdated wavelength references, and incomplete spectral coverage. Consequently, the full potential of the IAG atlas for determining precise convective blueshifts remains unrealized, highlighting the need for the refined analytical methods applied in this project.

1.3   The IAG spatially resolved quiet sun atlas

In 2023, Ellwarth and colaborators [7] published the *Institut für Astrophysik und Geophysik* (IAG) spatially resolved quiet sun atlas, also obtained with the FTS *Fourier Transform Spectrograph* at Göttingen. This atlas has the advantage of its coverage from the disk center ($\mu = 1.0$) towards the solar limb ($\mu = 0$), where $\mu = \cos(\theta)$ with θ being the angle between the surface

normal and the observer's position. This spatial resolution enables the study of how convective blueshifts vary across the solar disk due to changing projection angles, a dependency that cannot be observed in other stars.

The principal objective of this project is to characterize the solar granulation pattern by treating the Sun as any other star. To achieve this, the disk-integrated IAG solar flux atlas serves as our primary data source. However, a precise analysis of the relative velocities in this integrated light requires correcting for the center-to-limb variations that are uniquely quantified by the IAG spatially resolved quiet Sun atlas.

1.4   Motivation

In the first semester of 2025, Manuel Fuentes, a physics student at the Universidad de los Andes, implemented these improvements in a computational project focused on the visible spectral range. By developing enhanced measurement techniques and employing a carefully curated line list that fully covers the visible range with updated wavelength references, Fuentes achieved significantly sharper granulation patterns than previous analyses. This work demonstrated that proper line selection and modern wavelength standards can reliably extract convective signatures from high-quality solar spectra.

Under the guidance of Professor Benjamin, the present project extends the analysis into the near infrared range. This region contains spectral lines that originate from deeper photospheric layers. Although these lines are consequently weaker, they represent a rich source of information. However their analysis requires an adaptation of the existing measurement methodology. A key objective was to adapt these methods to enable the characterization of solar dynamics through granulation patterns in the near infrared range. This project also extends previous efforts by measuring the line asymmetry and broadening, other spectral signs of granulation beyond conevtive blueshift; and exploring how these phenomenona depend on the wavelength range.

By addressing these challenges, this project aims to produce a robust characterization of the solar granulation pattern and new insights into the photosphere's dynamics. These efforts are

guided by the central research question: What are the direct spectroscopic consequences of solar convection?

ADD VALT AS REFERENCE FOR OTHER COEFFICIENTS AND EXPLAIN THAT NAVE HAVE VALUES OF EXCITATION POTENTIAL

Chapter 2

Literature Review: Convective motion in the Sun

As previously mentioned, David Gray has significantly advanced the study of granulation patterns in the solar photosphere, with a particular focus on measuring relative velocities with high precision. This chapter explores the three signatures of convective motion in the Sun photosphere, and how this reveals the hydrodynamics on this outermost layer.

2.1 The solar interior and the solar outer atmosphere

The Sun is classified as a yellow dwarf star of spectral type G2V. Its chemical structure is primarily composed of a large fraction of ionized hydrogen and a smaller proportion of helium. What makes the Sun unique in astronomical studies is its proximity to Earth,which allows for detailed observation unmatched for any other star. Structurally, the Sun is divided into two main regions: The solar interior and the solar outer atmosphere.
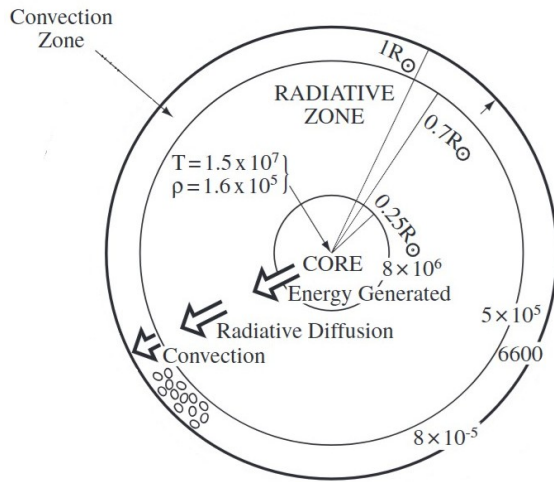
(a) The interior structure of the Sun. The convection zone is responsible for the general movement that characterizes the third signature.
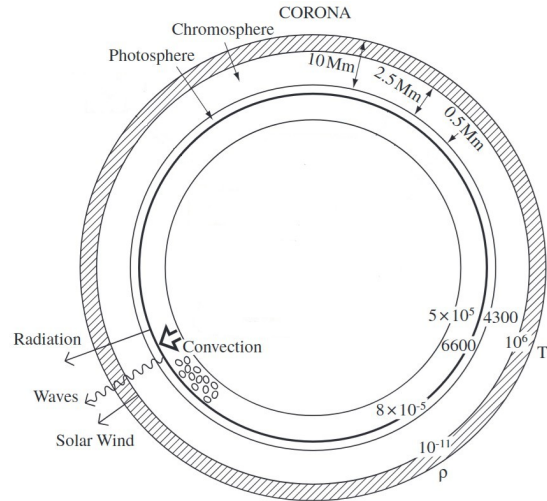
(b) The outer structure of the Sun. The photosphere is the layer of the sun where the convection cells overshoot from the convection zone.

Figure 2.1: The general structure of the Sun. Images modified from [1].

As illustrated in Figure 2.1a the overall structure of the solar interior is core, radiative and convective zone. Moving outward through these layers, both the density and temperature decrease significantly, as the energy is slowly transferred outwards by radiative diffusion. In the core, where energy is generated by thermonuclear fusion, standard models estimate a temperature of 1.6×10^7 K and density to 1.6×10^5 kg/m^3.

The extreme conditions in this region maintain the central material in a plasma state, functioning like a massive nuclear reactor.

This characteristic high density allows the absorptions and remissions of photons that make this zone highly opaque. This process, known as radiative diffusion, slowly transfers energy outward and progressively shifts the wavelength of the radiation from high-energy $\gamma-$rays to the visible light that eventually escapes.

On the other hand, Figure 2.1b illustrates the overall structure of the solar outer atmosphere which consists of the photosphere, chromosphere and corona. In these layers, the density decreases rapidly with height above the solar surface. The temperature decreases to a minimum of approximately 4300 K in the upper photosphere before rising through the chromosphere and

transition region to millions of degrees in the corona. Thereafter, the temperature falls slowly expanding outwards as the solar wind.

The most relevant layer for this project is the photosphere. This thin layer of plasma that emits most of the solar radiation and a continuous spectrum. When the continuous light passes through the overlying chromosphere, specific wavelengths are absorbed, resulting in the characteristic Fraunhofer lines superimposed on the continuum [1]. This characteristic allows observing the convection in the spectrum.

The target layers of this study are the convection zone and the photosphere, which will focus in further sections.
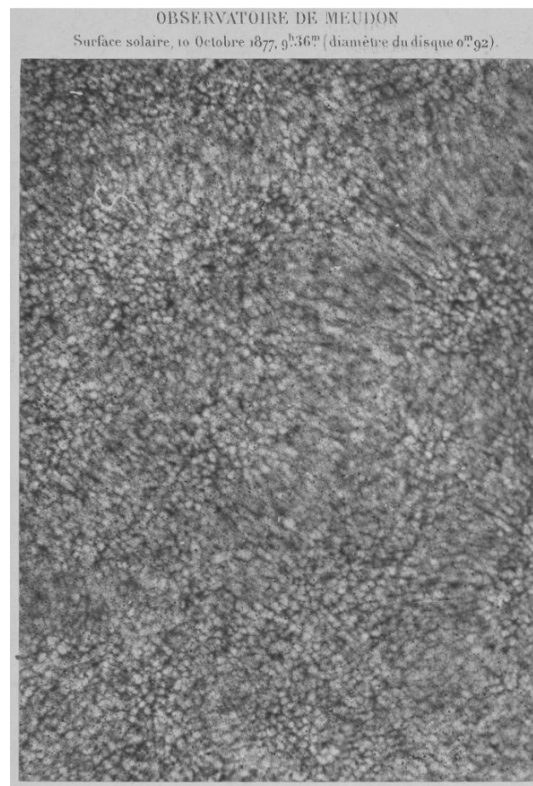
Figure 2.2: The first clear photograph of the photosphere where the granulation pattern is visible. Image taken from [2].

In 1885 Janssen obtained the first clear photograph of photospheric granules [2] providing the initial evidence for this granularar pattern (see Figure 2.2) This was the starting point for different studies across the pattern of these granules. In 1930, Unsöld theorized that the layers

14

beneath the photosphere should be convective unstable [4]. This hypothesis was later supported when Plaskett related the observed granules to the convective cells studied in Bénard's laboratory experiments [14]. In this analogy, a fluid heated from below develops rising elements of hot gas that transport heat to the surface.

These convective elements are known as granulation, with each individual region referred to as a granule. Typical granules span approximately 700 km and have short lifetimes, lasting between five to ten minutes. The understanding of granules as convective cells provided direct evidence for the existence of a zone responsible for convective motion beneath the photosphere.

2.2 The solar convection Zone

The convective zone, where dynamic plasma motions occur, begins at approximately $0.86R_\odot$. The great temperature gradient across this layer allows the convective process [1].

As previously mentioned, convection is driven by fluids heated from below representing hot rising gas elements or *convective cells* transporting heat to the photosphere [14]. In the solar context, convection takes place in a highly compressible and stratified gas. This physical regime leads to determine the conditions required for convection to occur and the resulting dynamics of the granules [4].

2.2.1 Dynamics of solar convection

From the core, He nuclei is built from H nuclei in the proton-proton chain as Equation (2.1) refers.

$$4\,^1\mathrm{H} \rightarrow\,^4\mathrm{He} + 2e^+ + 2\nu + 26.7\mathrm{MeV} \tag{2.1}$$

The proton-proton chain reaction in the core liberates approximately 26.7 MeV of energy in the form of high-frequency γ-rays, and 0.5 MeV of energy in the form of neutrinos. However, the strong Coulomb repulsion between positively charged nuclei, which increases with the product of their nuclear charges, means that only the lightest elements have appreciable fusion probabilities.

As energy is transported outward, photons are frequently absorbed and re-emitted. This process reduces the radiative conductivity, which in turn increases the temperature gradient [4]. When the transported energy reaches the low photosphere, a portion of the radiation escapes into space, and the plasma returns to a state of convective stability [1]. These conditions establish the onset of convection.

Consider a granule of plasma in local hydrostatic equilibrium with its surroundings, characterized by radial profiles of pressure $P(r)$, density $\rho(r)$, and temperature $T(r)$. If the granule's temperature is increased to a value T', it will expand adiabatically to maintain pressure equilibrium, thereby decreasing its density relative to its surroundings.

This lower-density gas then experiences a buoyancy force, causing it to rise. The buoyancy force persists until the granule's density matches that of its new surroundings after traveling a mixing length l. Let T'_n be the temperature of the rising element and T_n the temperature of its new surroundings. The difference between the adiabatic gradient of the element and the radiative gradient of the surroundings governs the convection, as described by Equation (2.2)

$$T_n = T + \left(\frac{dT}{dr} \right)_R l \quad \bigg| \quad T'_n = T' + \left(\frac{dT}{dr} \right)_{ad} l \tag{2.2}$$

Where R refers for radiative temperature gradient and ad for the adiabatic temperature gradient. Convection occurs when the radiative gradient becomes steeper than the adiabatic gradient. Since we have assumed radiative equilibrium, the R denotes the gradient present in the stellar atmosphere.

The onset of convection leads to the inequality (2.3), where two conditions can arise: The convection pattern is established when adiabatic gradient exceeds the radiative gradient; otherwise, the layer is stable and energy is transported by radiation.

$$-\left(\frac{dT}{dr} \right)_R > \left(\frac{dT}{dr} \right)_{ad} \tag{2.3}$$

If the convective pattern is established, the element continues to expand adiabatically as it rises, driven by buoyancy. Otherwise, if the layer is stable, the element will contract, becomes heavier than its surroundings and begins to move down toward its original position.

This onset of instability, when the vertical temperature gradient is too large, is formally de-

scribed by the Schwarzschild criterion for convection.

2.2.2 The Schwarzschild criterion

Taking the element described before, now suppose an elementary parcel of material displaced so slowly that remains in horizontal pressure equilibrium (see Figure 2.3).
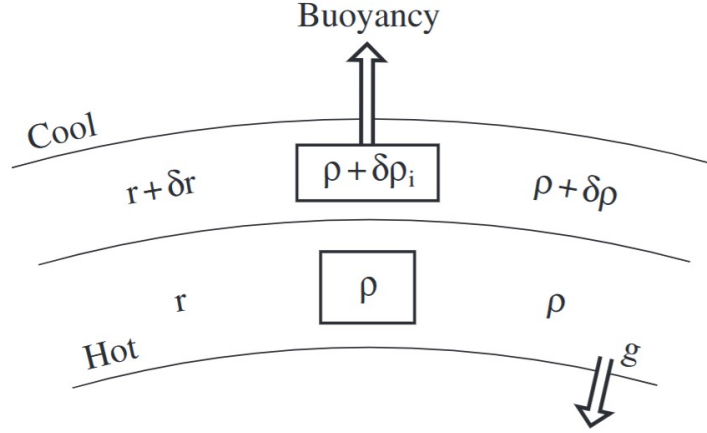
Figure 2.3: Diagram for the parcel of material displaced so slowly that remains in horizontal pressure. Image taken from [1]

If the motion is adiabatic there is no heat exchange with surroundings, the pressure and density of the rising element are adiabatic. This generates a criterion for the presence of convection known as the Schwarzchild criterion (2.4).

$$-\frac{dT}{dr} > \frac{\gamma - 1}{\gamma} \left(\frac{GM_\odot m}{r^2 k_B} \right) \tag{2.4}$$

Where k_B refers to Boltzmann constant; G the gravitational constant; $M_\odot$ the solar mass; m the mass of the granule; and γ the adiabatic index. The presence of convection reduces the temperature gradient from the higher value required for purely radiative transport to a adiabatic value [4]. The material and energy transported by this process ended on the low photosphere, where the granules exhibit different properties that will be examined in subsequent sections.

2.3 The Solar Photosphere

Since 1874, when Langley gave a detailed description of granulation on the photosphere, astronomers have studied the dynamics and reactions within Sun's outermost layer [1]. A distinct pattern of granules with dynamic behavior is apparent, where individual cells continuously emerge and disappear (see Figure 2.4).
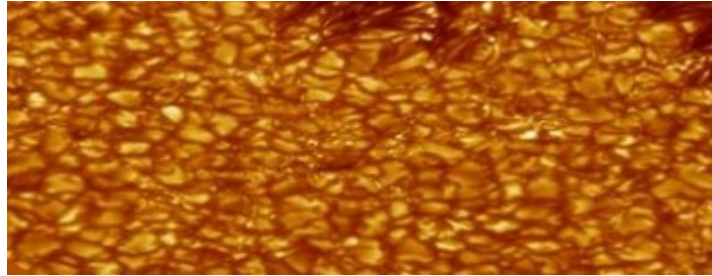
Figure 2.4: A view of granulation on the Sun's surface. The central regions exhibit blueshifts while the edges display redshifts. Image taken from [3].

The bright areas of granules correspond to regions where hot gas rises through the solar atmosphere. As this gas releases energy in the form of photons at the photosphere, it cools and subsequently descends, creating the darker regions of intergranular lanes [15].

Furthermore, high-resolution observations reveal that these granules are in continual motion (see Figure 2.5).
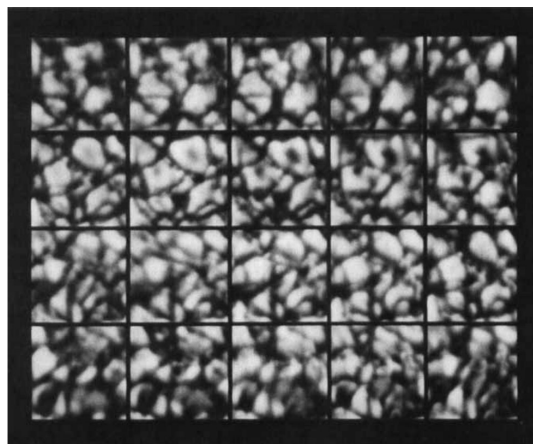
Figure 2.5: A time sequence showing granule evolution where the time intervals are about a minute. Image taken from [4].

This perpetual motion across the photosphere generates asymmetries in absorption line profiles.

2.3.1 Static photosphere: Limb darkening phenomenon

Because the temperature decreases outward through the photospheric layers, the observed intensity falls off towards the solar limb. Discovered by Halm in 1907 [5], this effect is known as *Limb darkening phenomenon*, which make the disk intensity profile to appear more squared at increasing wavelength (see Figure 2.6).
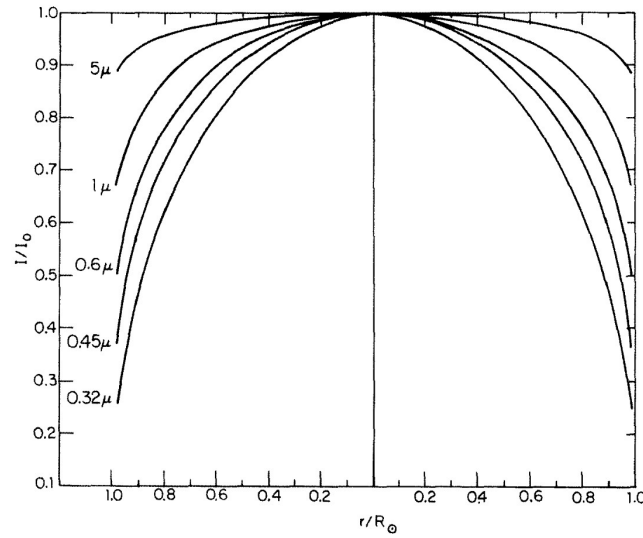
Figure 2.6: Squared profile for the disk intensity at increasing wavelengths. Image taken from [4].

The analysis of this effect provides a direct technique for determining the temperature structure of the photosphere as a function of depth.
For typical weaker lines, the convective blueshift diminishes toward the limb, with a net velocity change approximately of 400 m/s. As explain Ellwarth et al. observations closer to the limb pass through the atmosphere a shallower angle. This results in longer optical paths through high atmospheric layers, allowing the study of the layers where convective blueshift is less [7].

2.3.2   Dynamic photosphere: The C-curved profile bisector.

Analysis of granule dynamics reveals a height dependence of convective velocities: The vertical velocity of a rising granule decays less rapidly than its excess brightness. Changes in the granulation structure, contrast and velocity field around the spots and magnetic network have been inferred indirectly from observations of Fraunhofer line profile shapes [4]. A direct result of the correlation between brightness and velocity of granules is the characteristic C-curved line profile bisector observed in photospheric absorption lines (see Figure 2.7).
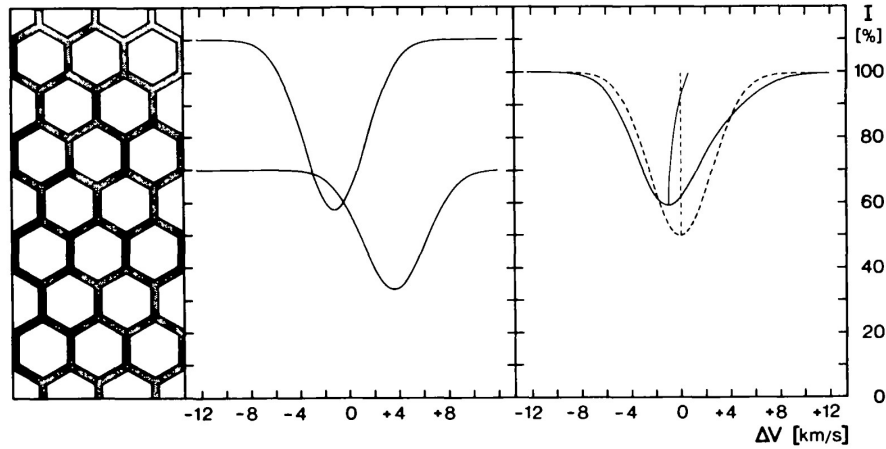
Figure 2.7: The C-curved line profile bisector. In the infrared shown to be less pronounced than violet range. Imagen taken from [5].

The formation of the C-curved line profile bisector occurs in three stages, corresponding to different heights in the photosphere.

First, the mid-depth portion of the line profile is formed in the brightest upflowing material, resulting in a blueshift. Then, the deepest part of the line core is formed higher up, in a region of decelerated upflow, producing a smaller blueshift. Finally, the line wings where the opacity is lowest, tend to be formed deepest in the cool material, resulting in a redshift.

This dynamic process induces characteristic perturbations in spectral lines, manifesting as line broadenings, line profile asymmetries, and line depth-dependent wavelength shifts known as the three signatures of convection [11].

2.4 The three signatures of convection

The signatures of convection in stars are described by Gray in his research (see [9, 8, 11] and references therein) as the principal characteristics to identify and treat the asymmetries due to convective motion.

2.4.1 First signature of convection: Line broadening

Due to the limb darkening phenomenon and atmospheric absorption, there exists two types of line cores: Strongest and weaker lines [11]. In general, stronger absorption lines exhibit more pronounced core curvature than weaker lines. This line core curvature C_c can be quantified by the second derivative of the line's intensity profile with respect to wavelength, evaluated at observed wavelength (see Equation (2.5)).

$$C_c = \lambda_{obs}^2 \left(\frac{d^2 p(\lambda_{obs})}{d\lambda_{obs}^2} \right) \tag{2.5}$$

In the near infrared range, the solar spectrum contains natural bands or groups of lines that are separated by regions of strong absorption from telluric elements. In other words, elements like O_2 and CO_2 that are absorbed by the atmosphere. This phenomenon modify the line core curvature of determining lines profiles, specially in the near infrared range.

2.4.2 Second signature of convection: Line profile asymmetry

As demonstrated by Nieminen [6], the asymmetry occurs because the c-curved profile bisector reflects velocity variations and a bisector slope (see Figure 2.8).

21
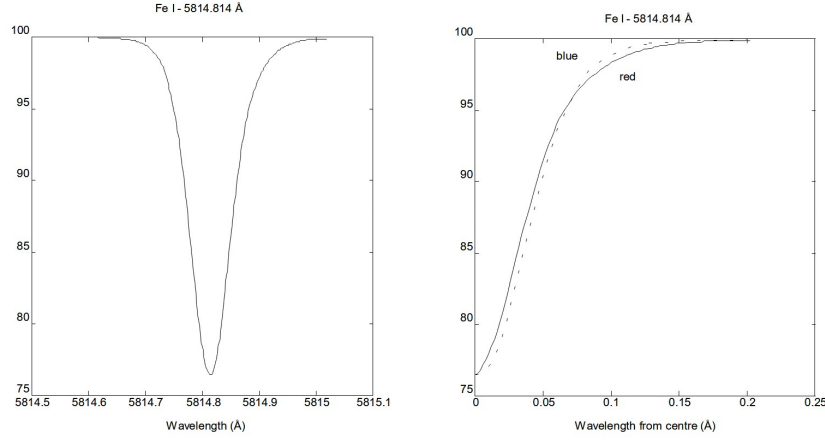
Figure 2.8: Asymmetries on an average absorption line. Can be observed the differences in intensity redshift profile. Image taken from [6].

According to Kirchhoff's laws, absorption line formation requires lower temperature conditions, which are found precisely in the Sun's outermost atmospheric layers [15]. These regions not only provide the appropriate temperatures for absorption but also exhibit comparatively higher opacity. Those spectral lines from Fe I are particularly valuable for solar granulation studies due to their high abundance, minimal thermal broadening, limited isotopic variation and availability of accurate laboratory measurements of natural wavelengths [6].

These asymmetries imprinted on the Fe I lines can be quantified by analyzing their bisectors. A convenient method for this measures involves using the third derivative of the line profile, which provides the slope of the lowest end of the bisector (see Equation (2.6)).

$$-\frac{c}{\lambda_{obs}}\left(\frac{1}{3C_c^2}\right)\left(\frac{d^3 p(\lambda_{obs})}{d\lambda_{obs}^3}\right) \tag{2.6}$$

The slope of the line profile is defined as zero when the line profile bisector is vertical and the line core is symmetric. The relation is derived in appendixB.

Since most of stellar observations are made with lower-resolution spectrographs and often lower signal-to-noise ratios, there is a need to study granulation through its signatures. Gray and Oostra identified a form of line profile asymmetry observable under these conditions, known as the *flux deficit*. This phenomenon can be interpreted as flux imbalances on the redshifted side of the line profile, caused by a net loss of radiative energy.

22

To quantify this asymmetry, the authors proposed calculating the flux deficit by taking the difference between the observed, altered profile and a the granulation curve. By treating the altered line profile as an approximate representation of the third signature of convection, one can observe the flux difference interpreted as radiation [8].

2.4.3 Third signature of convection: Line depth-dependent wavelength shifts

Many studies across the years have detected and observed the phenomenon of wavelength shifts against the line depth, or as it is called, convective redshift. This behavior was shown to be more present in the weaker lines which are related to infrared and violet range.

2.4.4 Solar granulation pattern

The solar granulation pattern is a plot of relative velocity against line depth, as shown Figure 2.9.
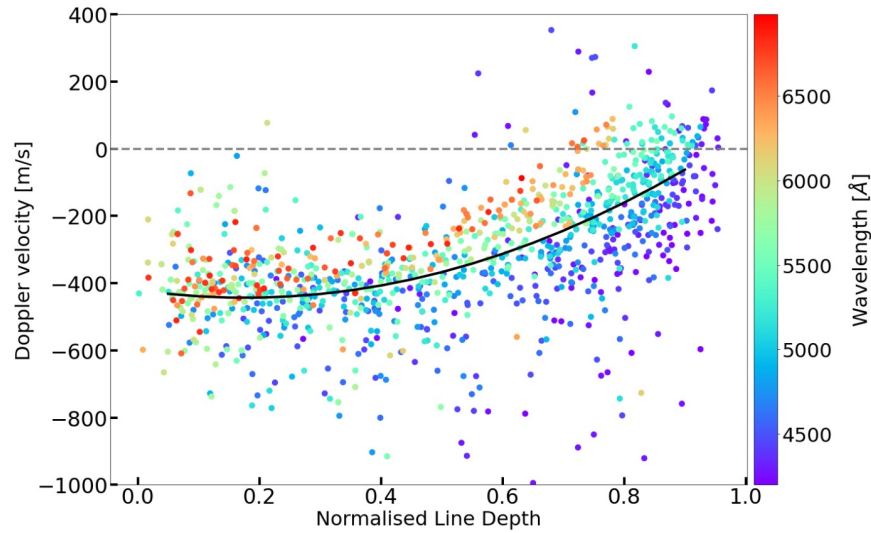
Figure 2.9: Granulation pattern for the IAG spatially resolved quiet sun atlas, is shown to have a strong blueshift in the weaker lines. Image taken from [7].

Notice in Figure 2.9 the wavelength-dependence os the pattern. The significance of the gran-

ulation pattern lies in its universality for solar-type stars; their patterns closely resemble the Sun's, differing primarily by a scaling factor (see [11]). Consequently, a detailed analysis contributes to the understanding and radiation of photospheric hydrodynamic models [5, 9]. However, a precise measurement of the granulation pattern requires a understanding of the convective blueshift phenomenon.

2.4.5 Convective Blueshift

When the Sun pushes material up through its outer layer, the spectrum exhibits a blueshift. As this material subsequently cools and falls back through the atmosphere, it produces a redshift, but emits less light, making the blueshift dominant.

That can be measured by the relativistic Doppler effect. This effect accounts for length contraction, as predicted by Einstein's theory of relativity. However, the measured negative redshift resulting from convective motions is known as *convective blueshifts* which are measured by the Equation (2.7).

$$v_r \approx c \left(\frac{\lambda_{obs} - \lambda_{rep}}{\lambda_{rep}} \right) \tag{2.7}$$

Since the strength of the convective distortions and shifts of spectral lines vary across the H-R diagram, we expect systematic errors in radial velocities [9].

2.4.6 Chromodependence characterization

Recent emphasis on measuring the granulation pattern has led to new interpretations of line depth-dependent wavelength shifts.

Gray and others authors have cualitatively explained the line-depth dependence on convective blueshift. Shallow lines come preferably from deep photospheric layers where convection is strong, so the convective blueshift is great. As long as deep lines come preferably from superficial layers, where gravity has slowed the convection and the blueshift is small. However, an explanation of why diagonal trend depends on color, or chromodependence along te line depth, has not been found.

In 2018, Gray and Oostra attempted to establish a standard curve determined by a third order

polynomial fit to the solar granulation pattern (see Figure 2.10).
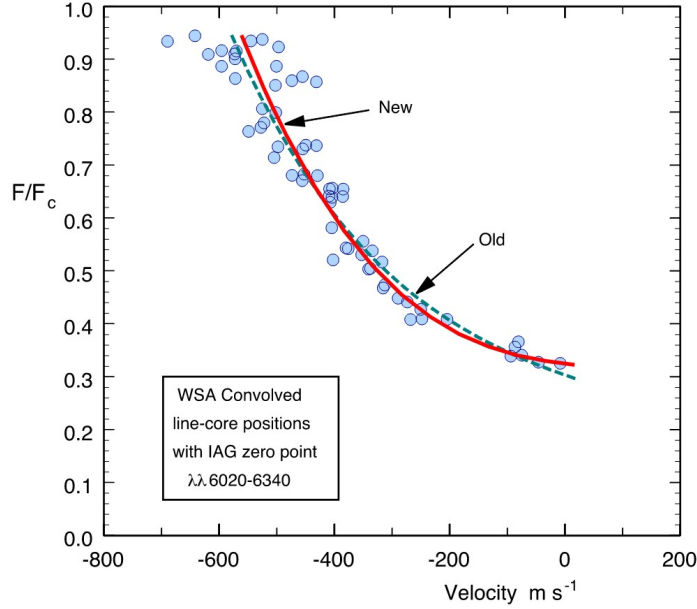
Figure 2.10: Standard curve proposed by Gray and Oostra on the spectral range the spectral range of 6020 Å to 6340 Å. Image taken from [8].

Nevertheless, the authors limited the spectral range of 6020 Å to 6340 Å, avoiding the chromodependence which becomes evident in a wider spectral range. This limitation motivates the present work to develop a strong characterization and give the methodology for dealing with this phenomenon.

A separate theoretical perspective, offered by Hamilton and Lester, attributes aspects of photospheric dynamics to rotation. The pronounced differential rotation with latitude observed seems to be the result of convective flows driven radially by the buoyancy force and deflected horizontally by the Coriolis force [4]. This rotation contributes to angular momentum through two forms: Meridional circulation and Reynolds stresses.
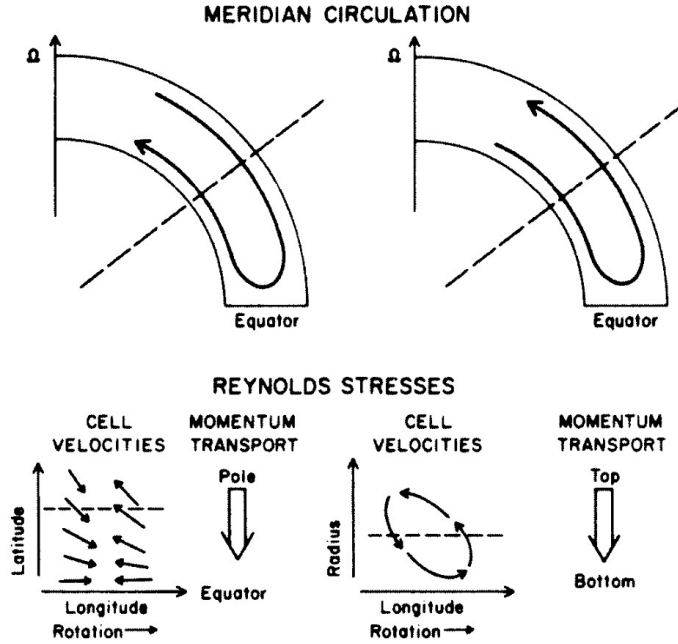
Figure 2.11: Contributions on angular momentum. Image taken from [4].

The first contribution involves axisymmetric meridional circulation (see Figure 2.11). In the absence of other transport mechanism, such a circulation would tend to spin up the poles and the interior, as the moving fluid conserves its angular momentum.

The second contribution, which tends to enforce solid body rotation, arises from Reynolds stresses associated with nonaxisymmetric convective motions. The mechanism can be understood by considering that, for equal velocities in the meridional plane, the flux of angular momentum per unit mass is greater toward the equator than away from it. This process depends critically on nonaxisymmetric convection, as it generates net fluxes of angular momentum in latitudinal and radial directions without a corresponding net mass flux. Neither buoyancy forces, which are strictly radial, nor pressure gradients, which must average to zero around the solar circumference, can directly influence the sun's axisymmetric rotation profile [4]. Therefore, the combined action of meridional circulation and Reynolds stresses is essential for shaping the observed differential rotation.

ADD BROADENING EFFECTS AND EXPLAIN THEM

Chapter 3

Methodology: The blend-free list of Fe I lines

Given the complexity introduced by convective motions on the spectrum, this project takes a computational approach leading, guided by Professor Benjamin and previous research. The analysis was conducted using the Python programming language. All data and code have been uploaded in a GitHub repository, allowing anyone interested to reproduce the results and verify the authenticity of the conclusions presented.

This project follows the methodology established in previous studies (see [5] and references therein), utilizing a selected list of Fe I lines from Nave [16]. As previously discussed, these lines are ideal for the calibration process due to their minimal thermal broadening and reduced susceptibility to other atmospheric perturbations.

3.1 Computational approach

The computational approach focuses on identifying the solar granulation pattern by calculating relative velocities from Fe I lines.

First, Fe I lines in the IAG Solar Flux Atlas and the IAG Spatially Resolved Quiet Sun Atlas using the blend-free list from Nave list of Fe I lines were identified [16]. For each identified line were selected bins of 0.1 mÅ around the closest minimal point to the associated value from

27

the Nave Fe I list. Beware, these points are not the observed wavelengths, just a reference to generate an observation window. Then, a fourth-order polynomial fit was adjusted due to the wavelength window and found the minimal point, whose represent the observed wavelength. The efficacy of this approach for quantifying asymmetry via the bisector slope is supported by [17]. For an optimal fit was used a z-score standardization on each line core, which is explained in appendixA. The observed wavelength from the polynomial fit was used to calculate the relative velocity. Finally, the values for the line core curvature (see Equation (2.5)) and the line core bisector slope (see Equation (2.6)) were found.

Furthermore, the variance of the observed wavelength was analyzed by altering the number of points used in the fourth-order polynomial fit. Figure 3.1 shows that this parameter set performs well in the visible spectrum. However, its performance degrades in the infrared, where the number of data points defining the line core is reduced compared to a typical line in the visible range.
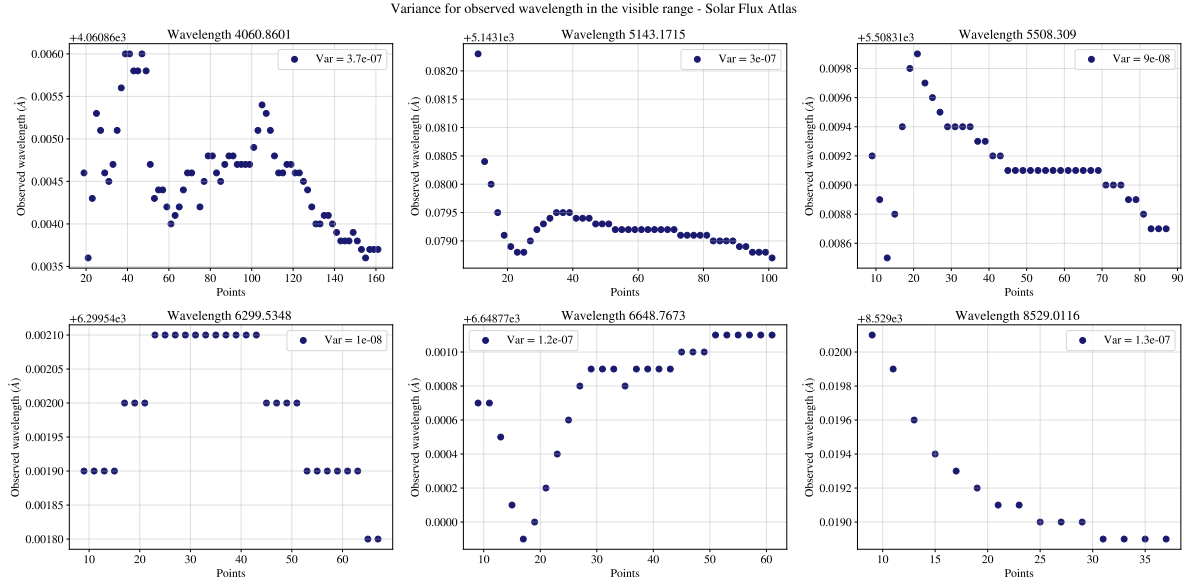
(a) Variance for several lines in the visible range for the Solar Flux Atlas.
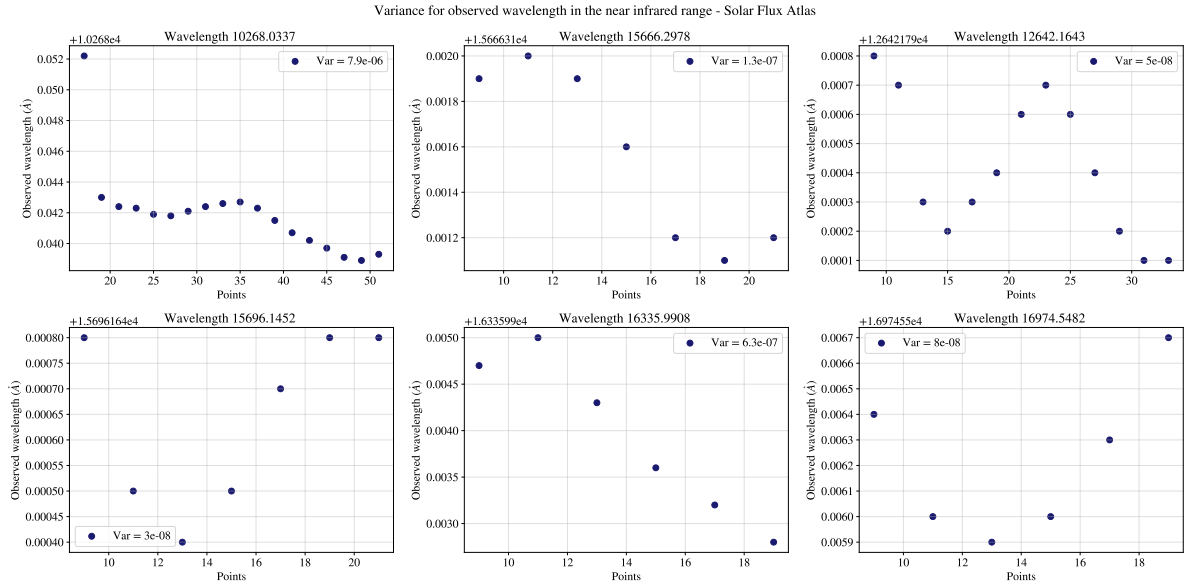
(b) Variance for several lines in the near infrared range for the Solar Flux Atlas.

Figure 3.1: Variance of the observed wavelength altering the number of points on the fourth order polynomial fit

IN PROGRESS Then, the same analysis was performed to the blueshift. And we study the variance of the window of the polynomial fit. IN PROGRESS

HERE:Add the uncertainty analysis of the mean varinace for the wavelength range that we use.

29

3.2   Blend-free Fe I line Nave list

The mentioned methodology implements the Nave list of laboratory-measured Fe I lines [16]. This list classifies lines with a quality grading (A, B, C, D), based on four wavenumber uncertainties ($\Delta\sigma$) and the corresponding wavelength uncertainties ($\Delta\lambda$). Where A denotes lines with error in wavenumbers less than 0.005 cm^{-1}; grade B less than 0.01 cm^{-1}; grade C less than 0.02 cm^{-1}; and grade D greater than 0.02 cm^{-1} All known blended lines and all lines measured only in grating spectra have been assigned the grade D [16].

However, not all the cataloged lines with grade A are clearly present in the solar spectrum, and within the near infrared range, many lines are severely blended. In collaboration with Professor Benjamin and Manuel Fuentes, we refined this initial list using different approaches to select the most reliable values.

3.2.1   Selection process for blend-free Fe I lines

The line selection process employed two approaches: Computational and visual. Initially, only quality A lines for the Nave list were selected. This group were subjected to four computational filters based on the properties of having a fourth-order polynomial fit for the line core.

The first filter takes into account the form of the C-curved line profile bisector. Lines whose c-curved bisectors exhibited excessive scatter, indicating a profile dominated by noise rather than a convective signature, were rejected.

The second filter selected lines whose curvature sign was consistent with an absorption line; this implies the coefficient of the fourth-order term needs to be positive.

The third filter ensures the selected lines represents an absorption curve by discarding closest points that more closely resemble slopes or continuum noise. The condition was discard lines which difference between extreme points of the fit were less than half of the line depth. This describe an absorption curve, and not a slope or noise.

The final filter required the absolute difference between the observed wavelength and the measured laboratory wavelength to be less than 0.025 Å. Larger discrepancies suggest misidentification or severe blending, rendering the calculated relative velocity unreliable. This threshold

is empirically supported by observations throughout the selection process and the statement for the mean velocity of the sun is 200 m/s to 600 m/s.

The final part of the selection process was a visual inspection to discard lines that were blended or absent from the solar spectrum. A custom visualizer (detailed in appendixC) was instrumental for this, allowing the simultaneously display of graphics related to dynamics aspects. This was particularly useful for selection lines in the near infrared range. The visual requirement focused on the geometry of the spectral line profile, its behavior on the three signatures plots.

The concluding part of the methodology was performed the plots which represents the three signatures of convection.

First of all, the granulation pattern (relative velocity), core curvature and core bisector against line depth was performed to all ranges in both atlases with the objective to observe the three signatures of convection. Subsequently, various parameters were plotted against line depth to specifically characterize the granulation.

MENTION THAT WE CHANGE THE LIMITS OF WAVELENGHT FROM REINERS TO STABLISH COPARISIONS WITH THE SPATIALLY NOW VISIBLE IS FROM 4000/7500 A AND NIR IS 7500/23000

Chapter 4

Results and discussion: The three signatures of convection

Our results were separated into three sections following the signatures of convection. All of them analyses these signatures around the main phenomenon of wavelength-dependence.

4.1 The first signature: Line broadening

4.1.1 Line depth-dependence on line core curvature

The line core curvatures were calculated following Equation (2.5), and plotted against line depth as shown Figure 4.1. In general, the behavior described in previous research was observed. For shallow lines, the line core curvature is proportional to depth as expected. Furthermore, for deep lines the line core curvature is reduced by saturation with strongly wavelength-dependence.
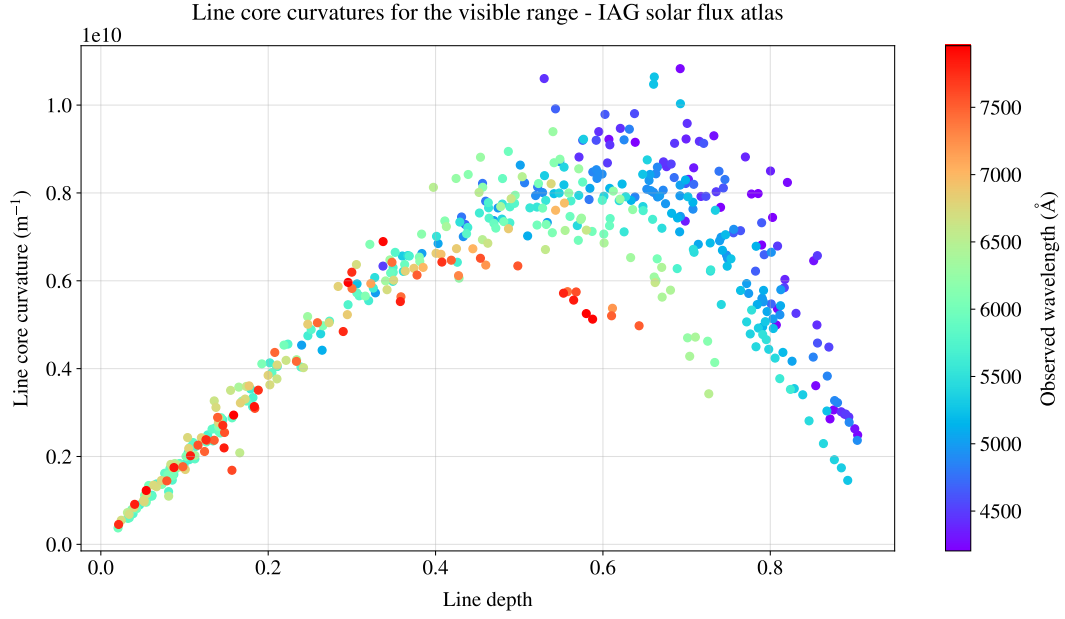
(a) Line core curvatures for the visible range. While shallow lines curvature is proportinal to depth, deep lines curvature is reduced by saturation with is strongly wavelength-dependence.
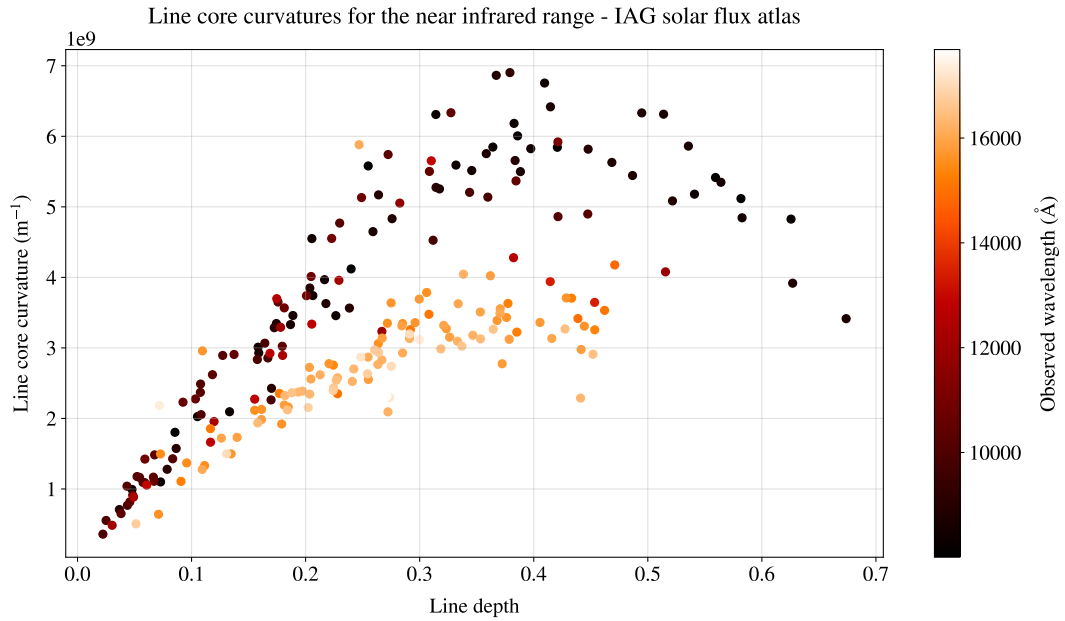
(b) Line core curvatures for the near infrared range. The plot shows a conspicuous partition around 14 000 Å

Figure 4.1: Line core curvatures for the IAG solar flux atlas separated in wavelength ranges.

As shown in Figure 4.1b the near infrared range exhibits a natural division at approximately

14 000 Å, a region dominated by telluric absorption lines from Earth's atmosphere. The division separates the J band, which refers to an atmospheric transmission window of 3000 Å centered on 12 500 Å; and the H band, which refers to an window of 3500 Å centered on 16 500 Å [18]. Plotting the entire spectral range of the IAG solar flux atlas, a clear line depth-dependence of the line core curvature as a function of wavelength is observed.
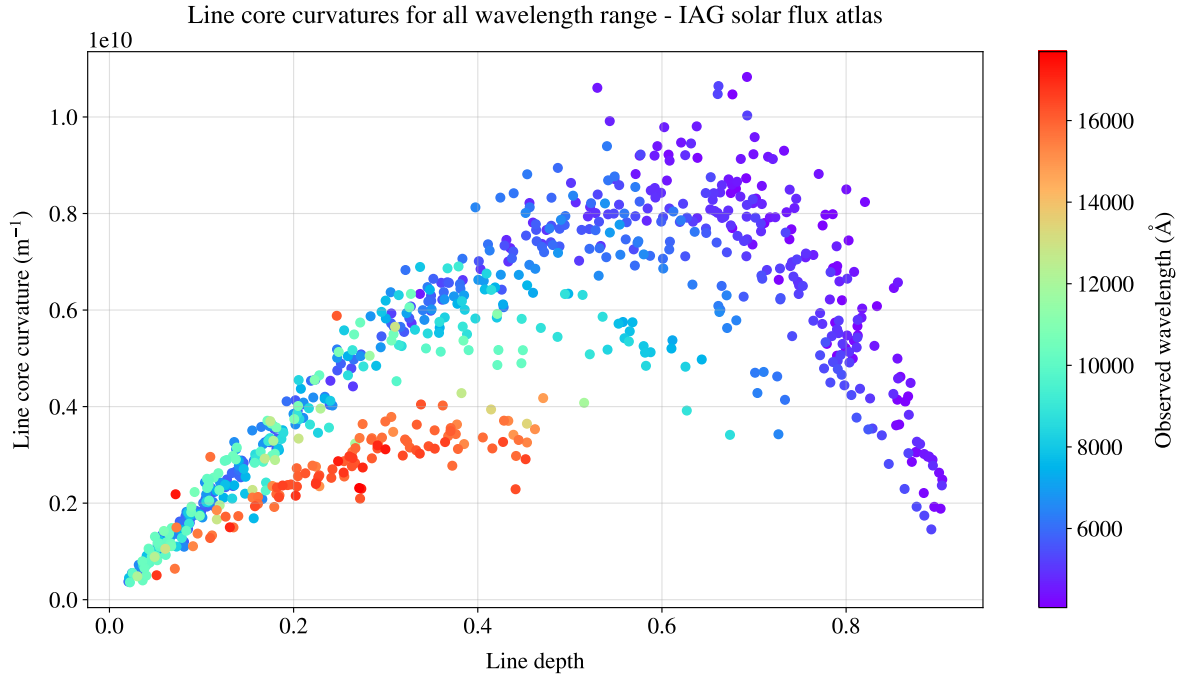
Figure 4.2: Line core curvatures in the IAG solar flux atlas. While the J band for the near infrared range adjust to the general shallow lines trend, the H band exhibit wavelength-dependence.

While the J band for the near infrared range adjust to the general shallow lines trend in Figure 4.2, the H band exhibit wavelength-dependence. Despite the line depth-dependent shifts along wavelength, the visible range of the IAG solar flux atlas exhibits a clear linear tendency for shallow lines (see Figure 4.2). Consequently, a linear fit was applied to the visible range for the IAG solar flux atlas in the range $0.0 - 0.1$ of line depth.
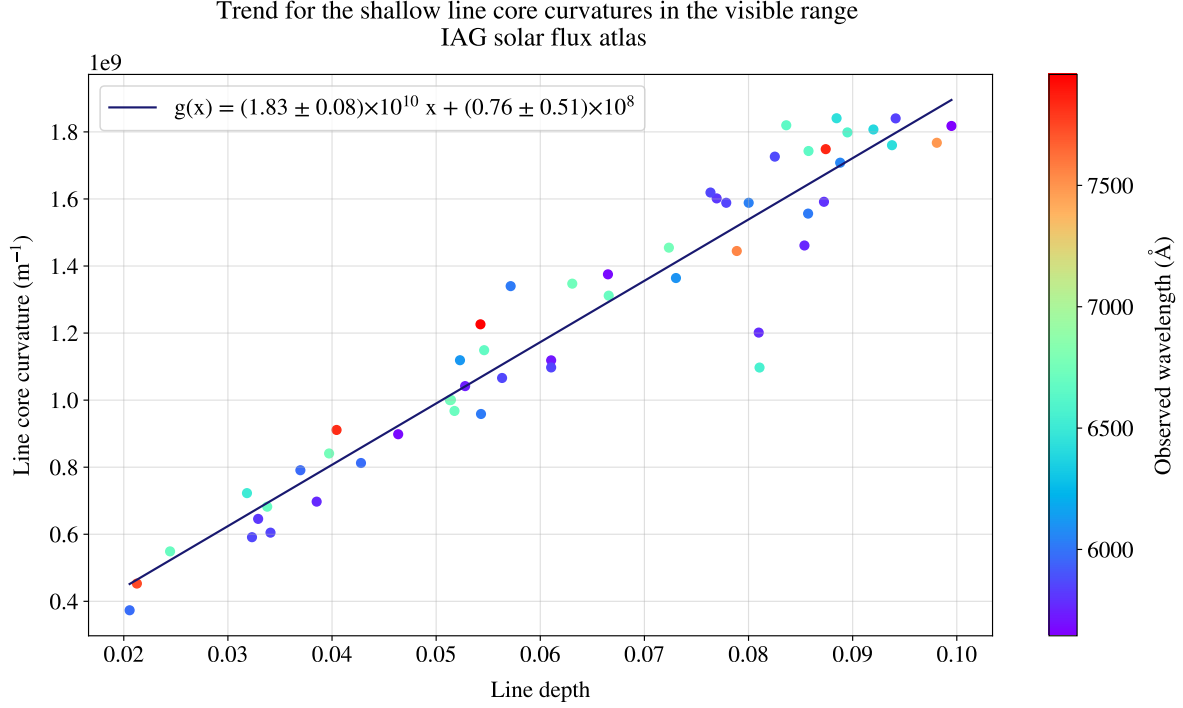
Figure 4.3: Linear fit applied to the range $(0.0 - 0.1)$ of line depth in the visible range of the IAG solar flux atlas.

As shown in Figure 4.3, the slope of the relationship has a value of $(1.83 \pm 0.08) \times 10^{10}$. The absence of wavelength-dependence in this spectral range indicates that line core curvatures have a net dependence on velocities (thermal, convective and rotational), with negligible influence from atomic effects. To confirm this statement, the line core curvature was also plotted for the visible range using the IAG spatially resolved quiet sun atlas at the solar limb $\mu = 0$ as shown Figure 4.4. In other words, this analysis uses light from the center of the solar disk, which is not affected by rotational Doppler broadening, thereby isolating the local effects.
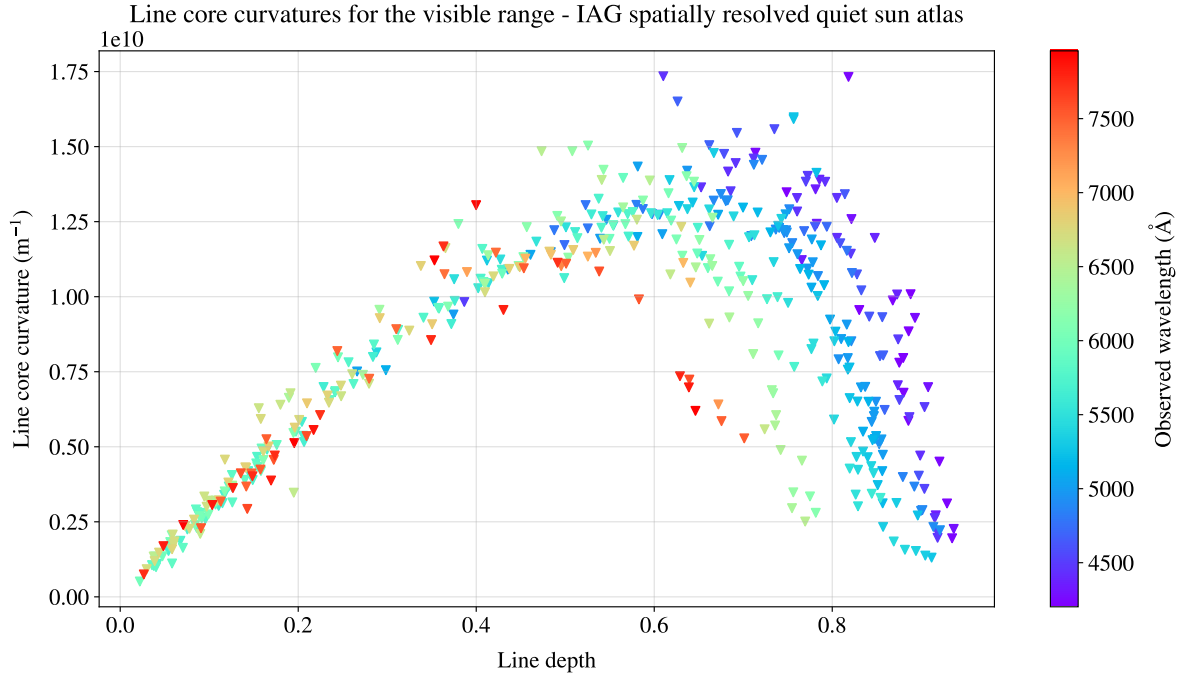
Figure 4.4: Line core curvatures for the visible range of the disk center data from the IAG spatially resolved quiet sun atlas.

A linear fit was applied taking the same range $0.0 - 0.1$ of line depth, the Figure 4.5 shows a value of $(2.94 \pm 0.16) \times 10^{10}$ for the slope.
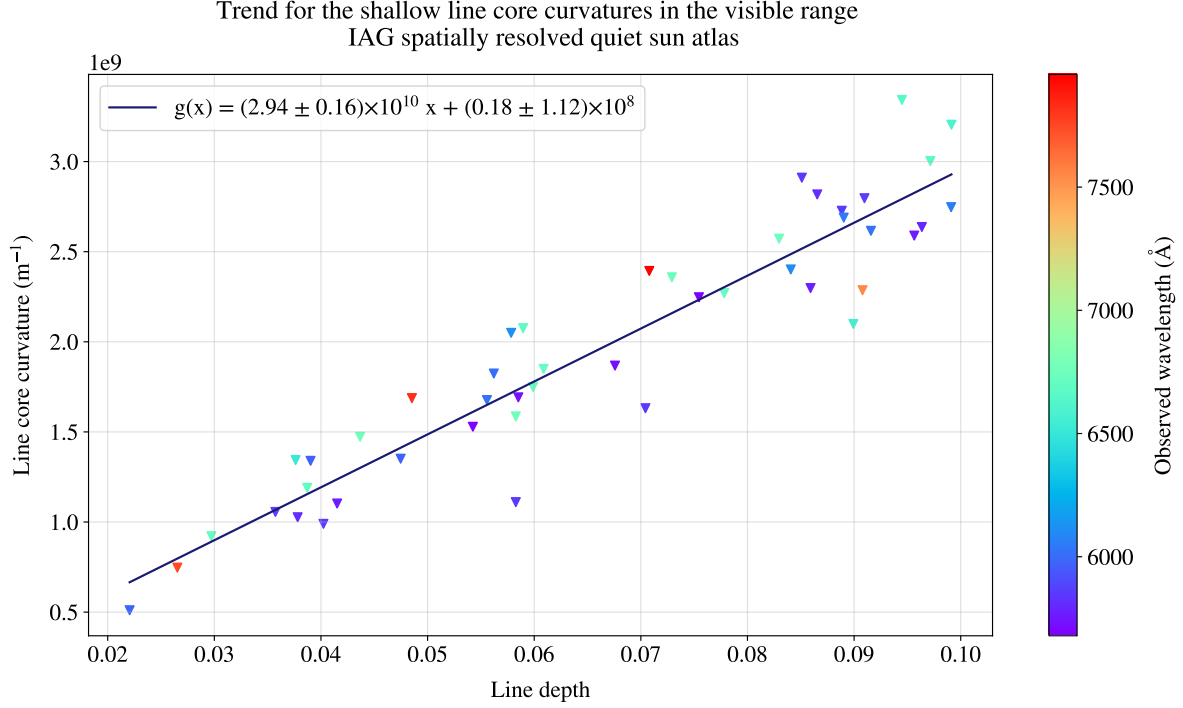
Figure 4.5: Linear fit applied to the range $(0.0 - 0.1)$ of line depth in the visible range of the IAG spatially resolved quiet sun atlas.

The result of found a greater slope in the center-disk confirm that rotation is a neligible effect for the line broadening. This allows deduce the variance of convection speed, knowing the thermal velocity.

IN PROGRESS.. As mention in chapter 3, we can induce from here the σ_{conv} as we the other parameters described in equation () and confirm that rotation is neligible. Benja comment: Here you could discuss all that can be learned about line broadening. For example: The slope of the disk-center spectrum doesn't depend on rotation, meaning it depends only on thermal broadening and convection. The thermal is known, so the variance of the convection speeds can be deduced. The slope of the flux spectrum is lower, because it includes rotation. The rotation is also known (but more work to calculate); but the three contributions can be assessed. Deeper lines deviate from the initial straight line, and this part is wavelength-dependent. The cause (s) should be discussed: Saturation in the deepest lines, but maybe other broadening effects (Lorentzian) may become important, and damping coefficients are somewhat related to

37

wavelength by atomic structure. IN PROGRESS..

4.2 The second signature: Line profile asymmetry

4.2.1 The line core bisector slope

As mention before, convection is the only mechanism that creates asymmetric line profiles. Consequently, the slope of the line core is a indirect line profile asymmetry measure, expressed as a velocity.

The line core bisector slope was calculated following the equation (2.6) and plotted against line depth, as shown Figure 4.6.

The shallow lines, due to their small depth, do not exhibit a fully developed C-shaped bisector. Instead, their bisectors shows as a positive slope. In contrast, deep lines experiences the convective blueshift in its totality, exhibit a negative bisector slope. The line depths in the middle range represent lines profiles which are not greatly affected by convection.
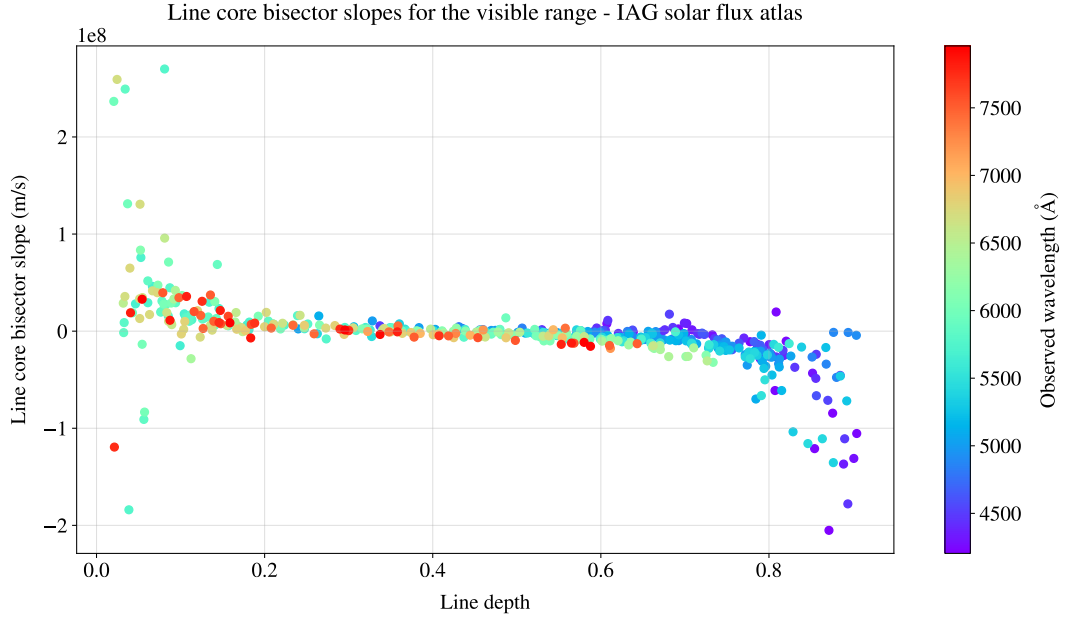
(a) Line core bisector slopes for the visible range.
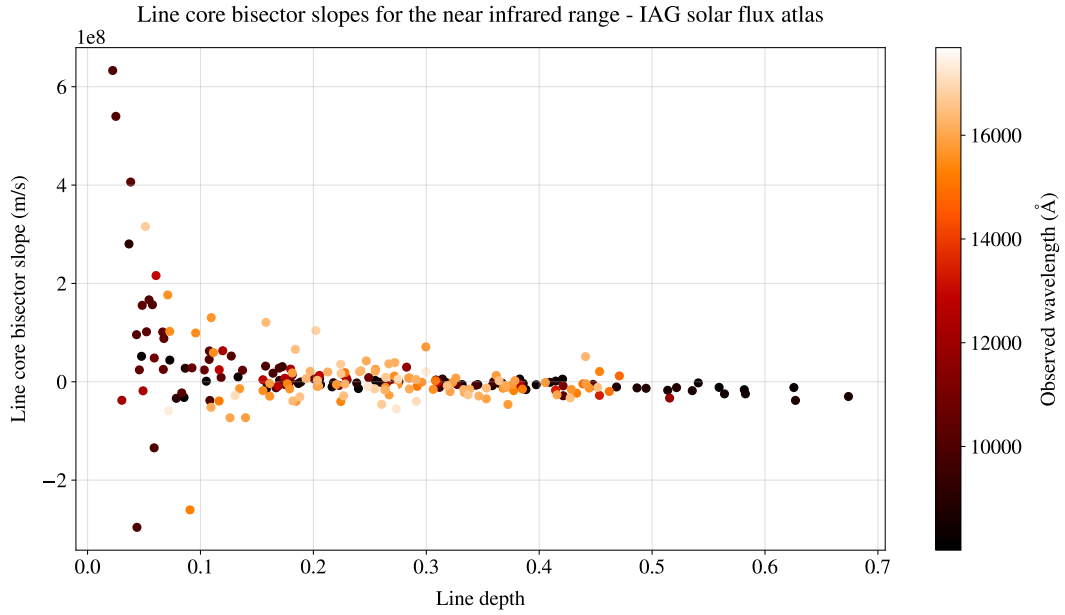
(b) Line core bisector slopes for the near infrared range.

Figure 4.6: Line core bisector slopes for the IAG solar flux atlas separated in wavelength ranges. The behavior of both plots is according to the C-curved shape of the line profile bisector affected by convection movement.

Searching for a comparision with the IAG spatially resolved quiet sun atlas, only the visible

range was analysed. Then a linear fit was applied to the line core bisector slope data in the line depth range of $(0.3 - 0.6)$ to quantify this transition, as shown in Figure 4.7.
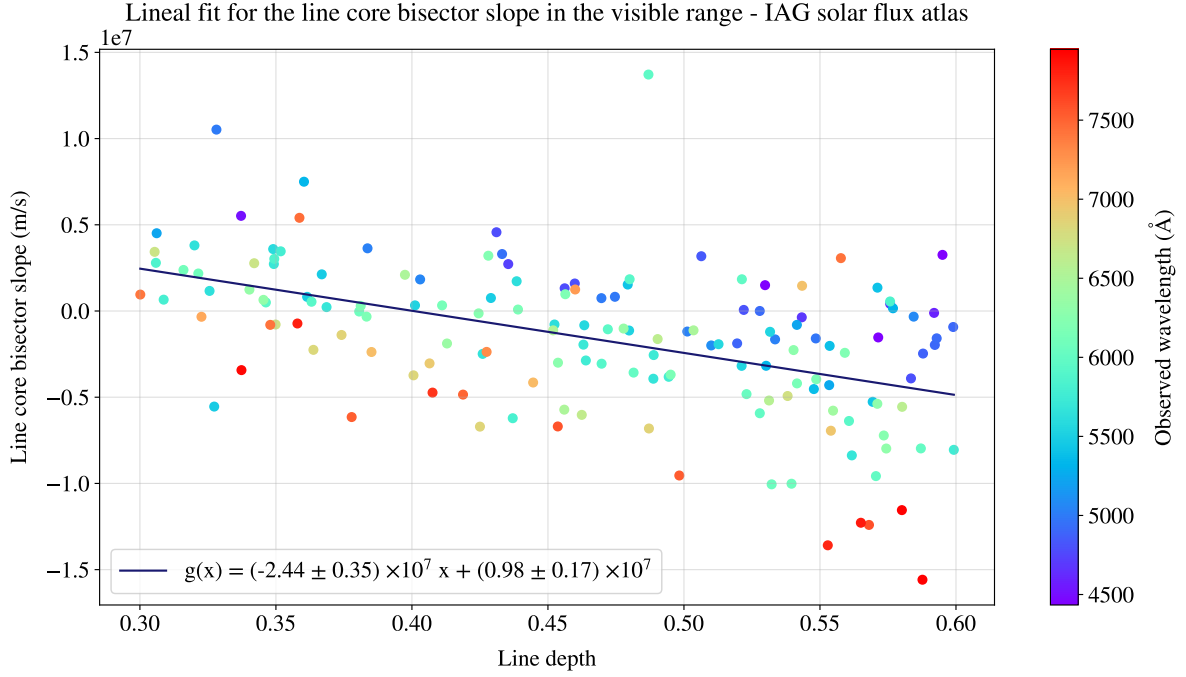
Figure 4.7: Linear fit adjusted to the range $(0.3 - 0.6)$ of line core bisector slopes in the IAG solar flux atlas, where is evident an wavelength-dependence.

As there is an evident wavelength-dependence along the line core bisector slopes, a point of comparision was searched comparing with the disk center spectrum (see figure 4.8).
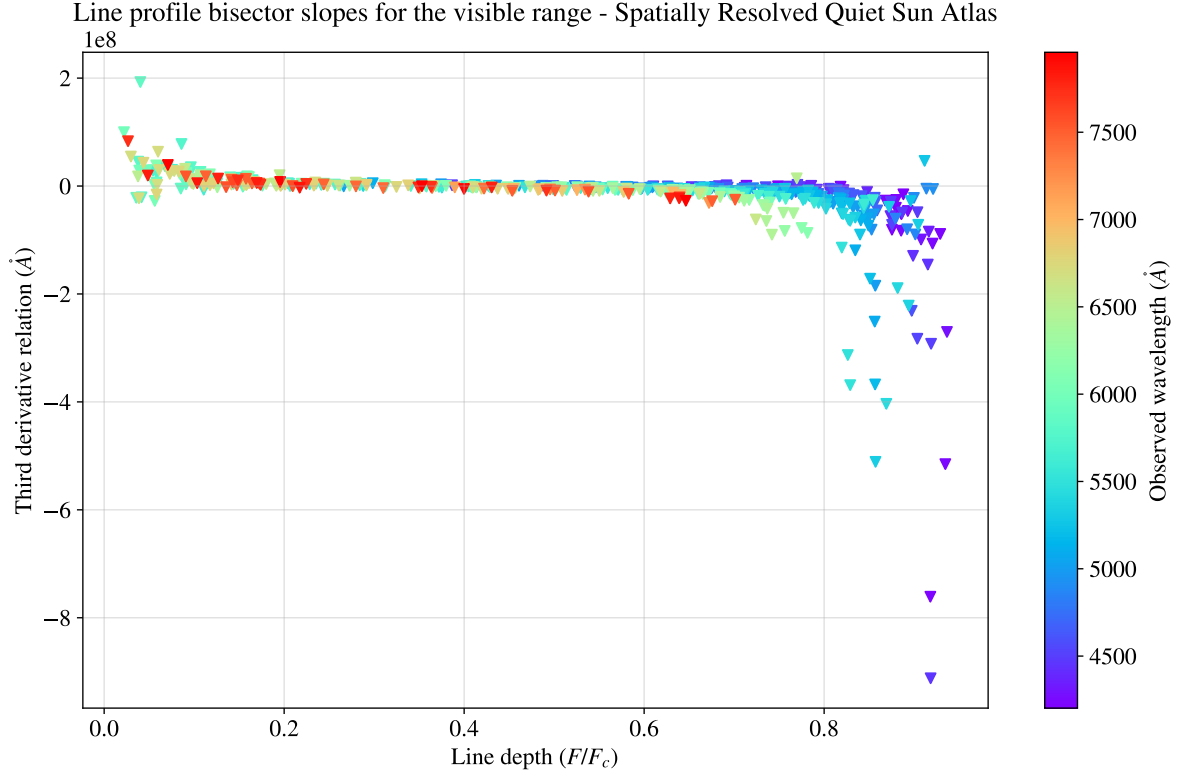
Figure 4.8: Line profile bisector slopes for the visible range in the IAG spatially resolved quiet sun atlas for $\mu = 0$.

The bisector slope derived from the disk center is smaller in magnitude compared to the integrated flux, despite both exhibiting the same characteristic trend (see Figure 4.9).
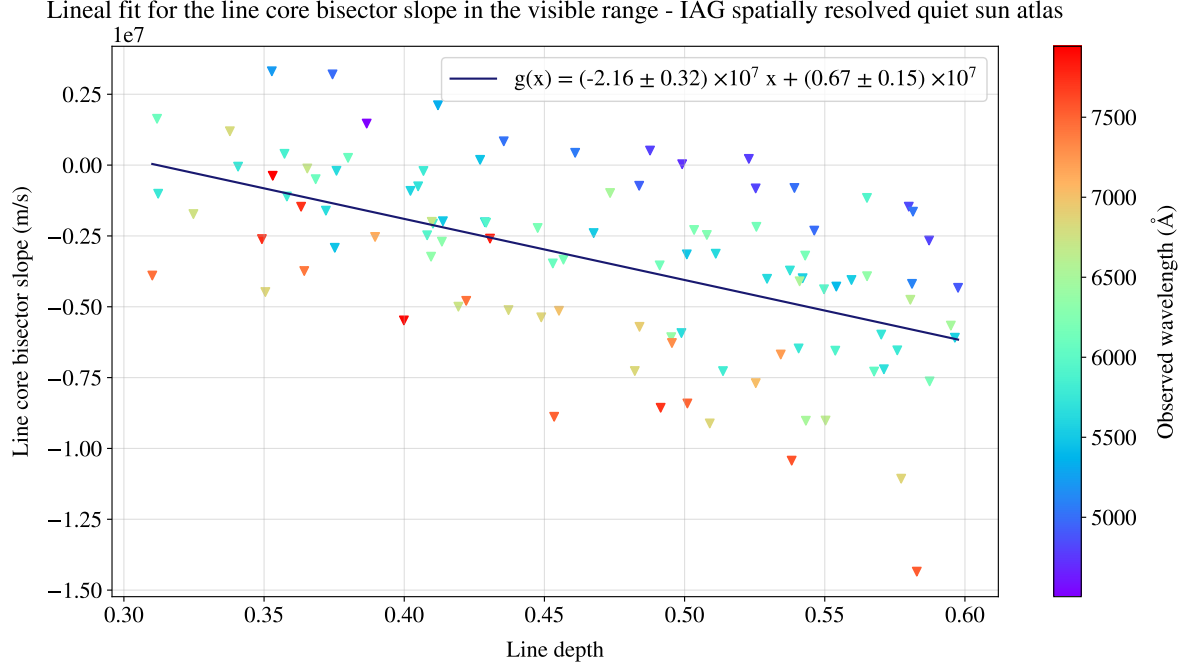
Figure 4.9: Linear fit adjusted to the range $(0.3-0.6)$ of line core bisector slopes int disk-center spectrum, where is evident an wavelength-dependence.

The phenomenon of chromodependence is evident of Figures 4.7 and 4.9, where the line profile bisectors slopes are organised by decreasing wavelength. This behavior is clearer on the disk-center spectrum than the disk-integrated flux spectra.

If line depth is separate into bins of 0.1 and plot the line profile bisector slope against wavelength, shifts in the line bisector slope become apparent as shown in Figure 4.10.
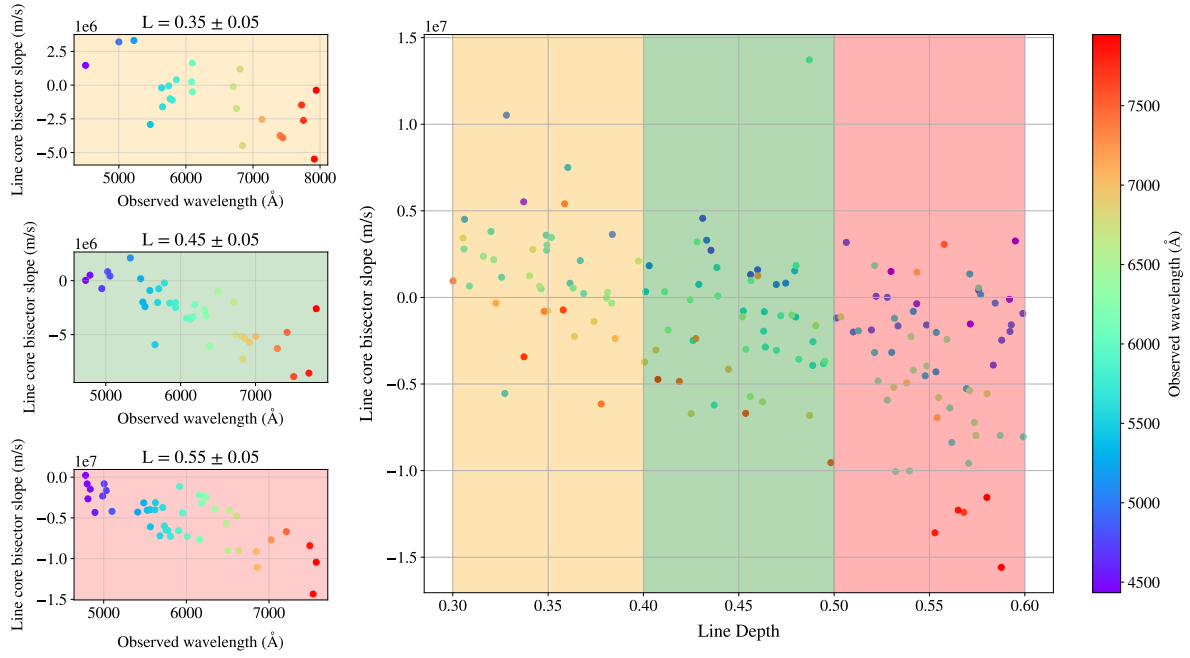
Figure 4.10: Line depth bins of 0.1, where wavelength-dependence of the slopes becomes apparent.

For the integrated flux spectrum was found that, for a fixed flux, the slopes decrease with wavelength (see Figure 4.11).
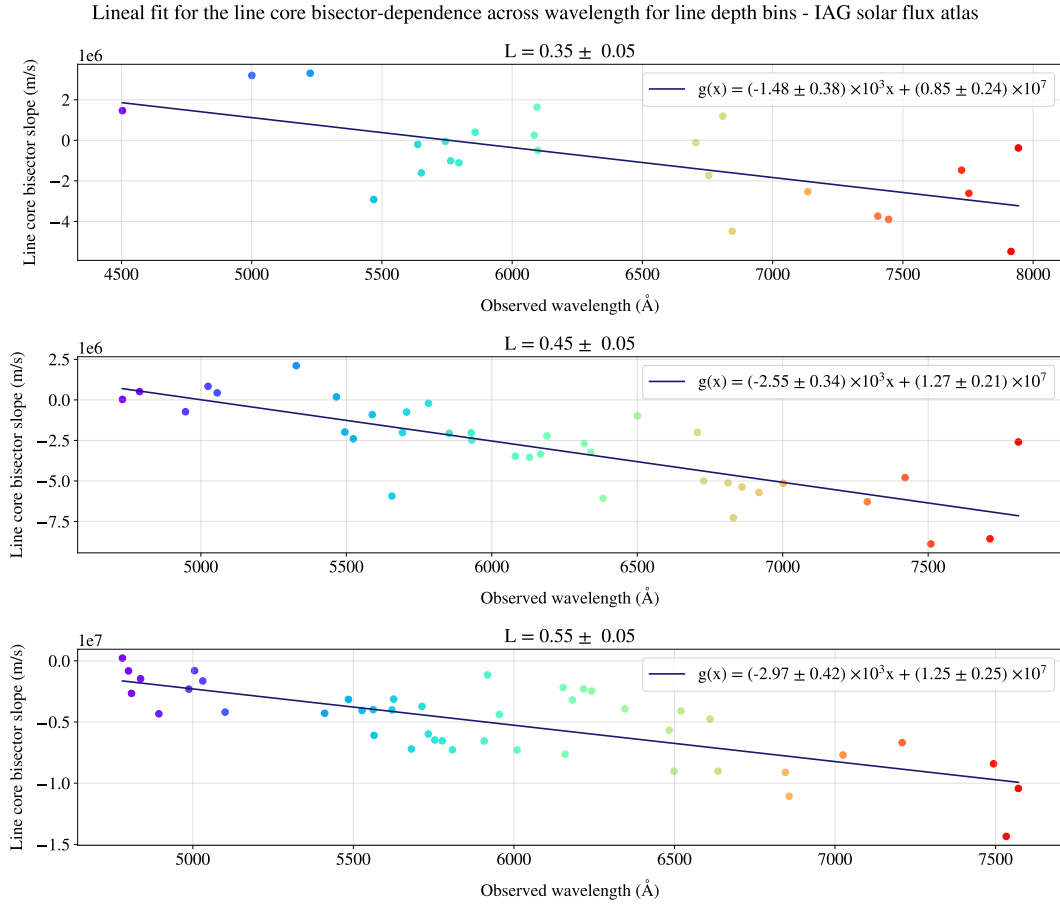
Figure 4.11: Individual plots of line core bisector slope shift across wavelength representing each bin of line depth for the IAG solar flux atlas.

The same analysis was performed on the disk-center flux and the same behavior was found (see Figure 4.12).
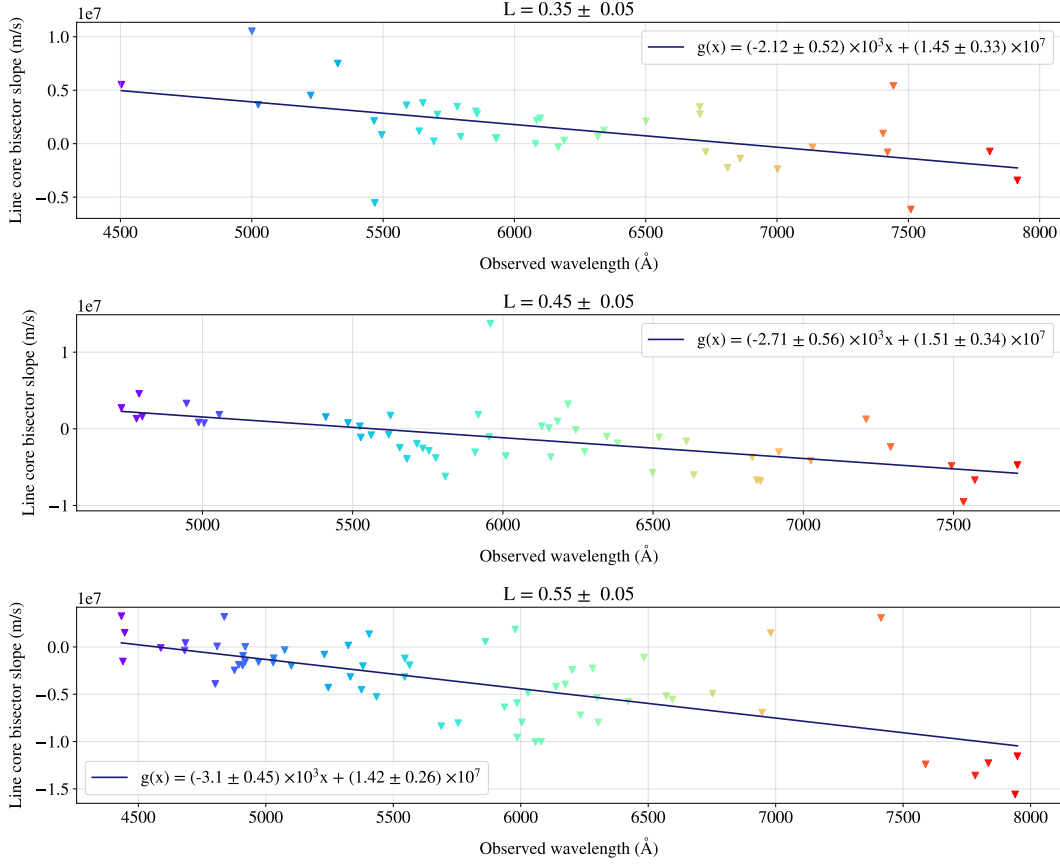
Figure 4.12: Individual plots of line bisector slope shift across wavelength representing each bin of line depth for the Spatially Resolved Quiet Sun Atlas.

IN PROGRESS.. So, for fixed flux we have chromodependence.. IN PROGRESS..

4.2.2 Flux deficit IN PROGRESS

Due to radiation, the redshift part of a line is displced on the flux, inducing a rotation on the c-curved line profile bisector. This phenomenon is called flux deficit. Hamilton and Lester [10] noticed that the behavior of the third signature mimics the line profile bisectors. The mean of line profile bisectors on ranges of wavelenght follows the behavior of granulation pattern, this last is discussed in the next section. Later, Gray and Oostra [8] show that the bisectors need to follow the granulation pattern as the form of we calculated velocities and bisectors.

For comparision with Gray and Oostra work, was taken the line 6254.2850 Å as shown in

Figure 4.13.
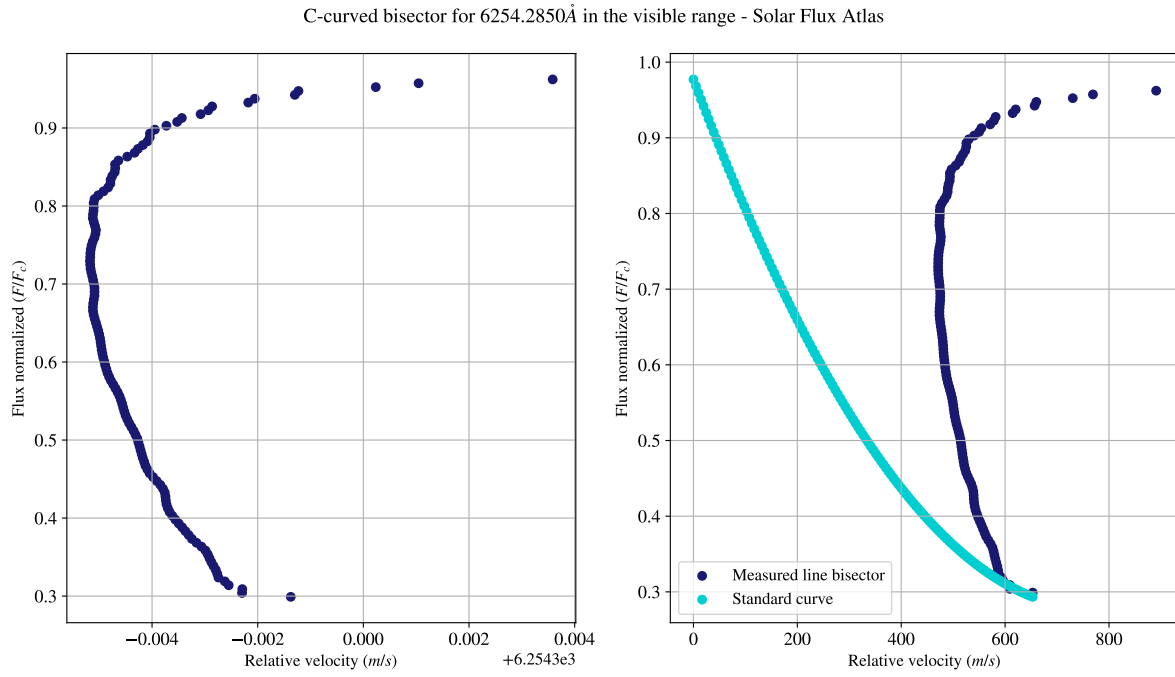
Figure 4.13: C-curved line profile bisector for the $6254.2850\mathring{A}$ and the standard curve for the green range from the third signature plot.

Following the same method, the figure 4.14 shows a flux imbalance described on the distribution and temperatures of the mean, the maximum and the RMS point of the bisector.
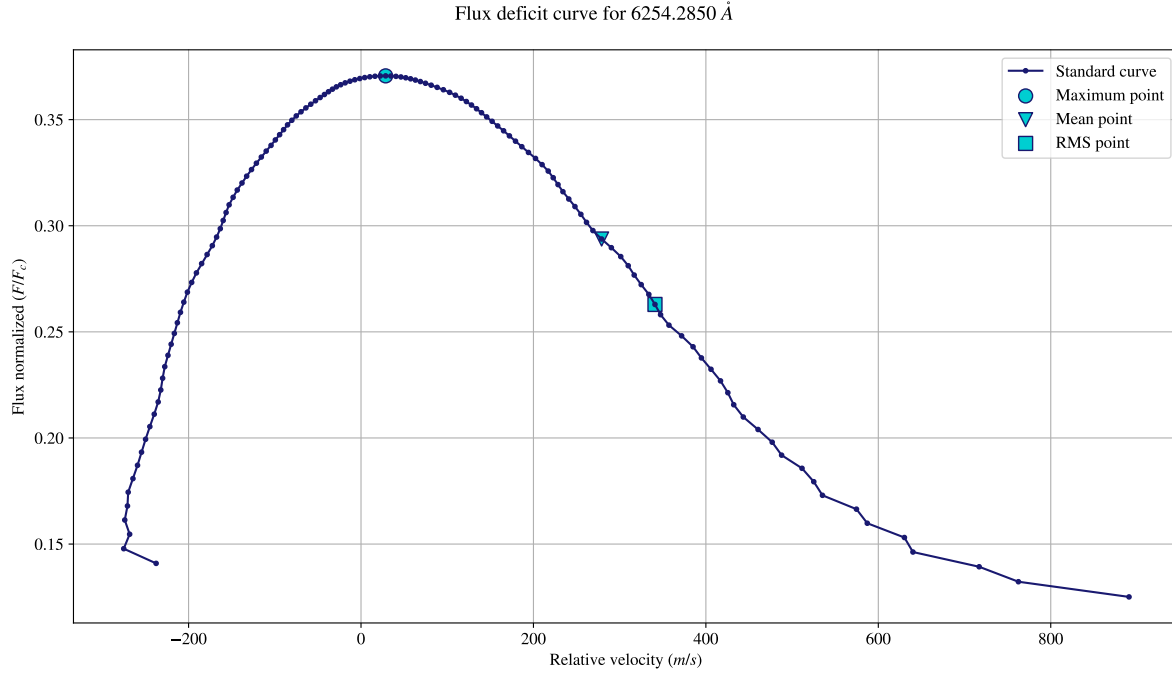
Figure 4.14: Flux deficit curve for the $6254.2850\mathring{A}$ and the temperatures of the mean, the maximum and the RMS point of the bisector.

The idea is add the flux deficit using the color curves and just report the velocities with the percent of the line corresponds that velocity. As we found the standard curves for all the ranges, the same analysis was realized for a random line in the range of the respective standard curve (im working on that). From this maybe get a description of line asymetry in the all visible range.

4.3 The third signature: Line depth-dependence on wavelength shifts

4.3.1 The granulation pattern

The granulation pattern is presented as the plot of relative velocity against line depth for the IAG solar flux atlas.

Granulation pattern for the visible range - IAG solar flux atlas

(a) Visible range for the IAG solar flux atlas.

Granulation pattern for the near infrared range - IAG solar flux atlas

(b) Near infrared range for the IAG solar flux atlas.
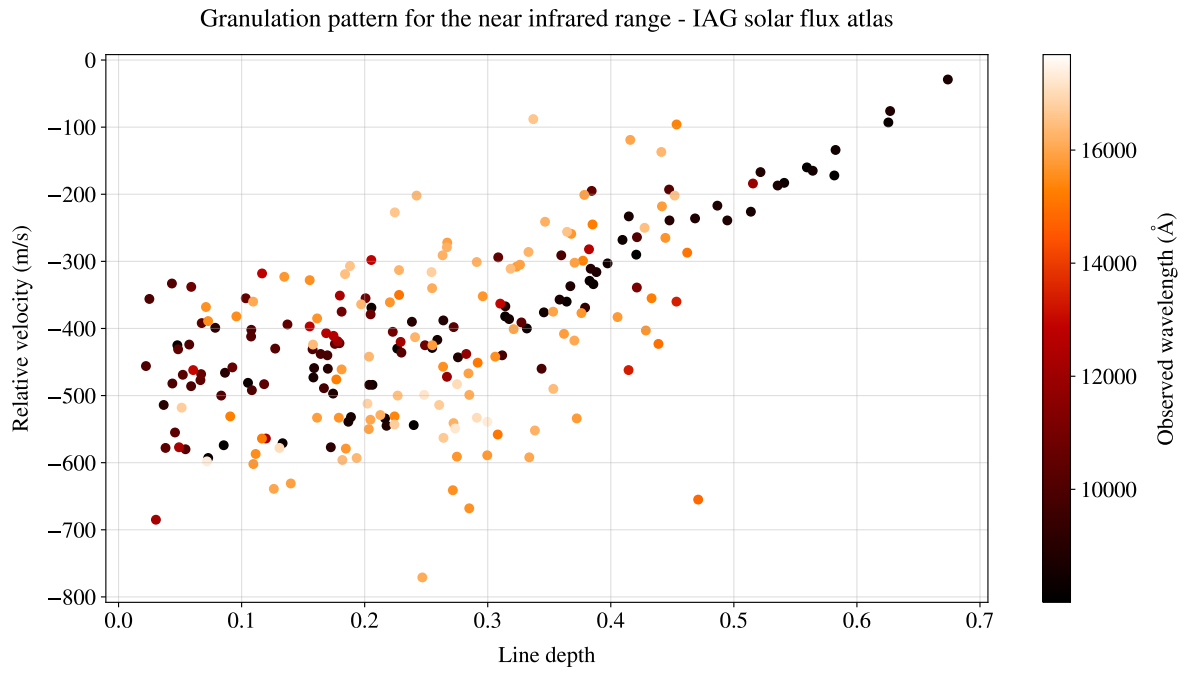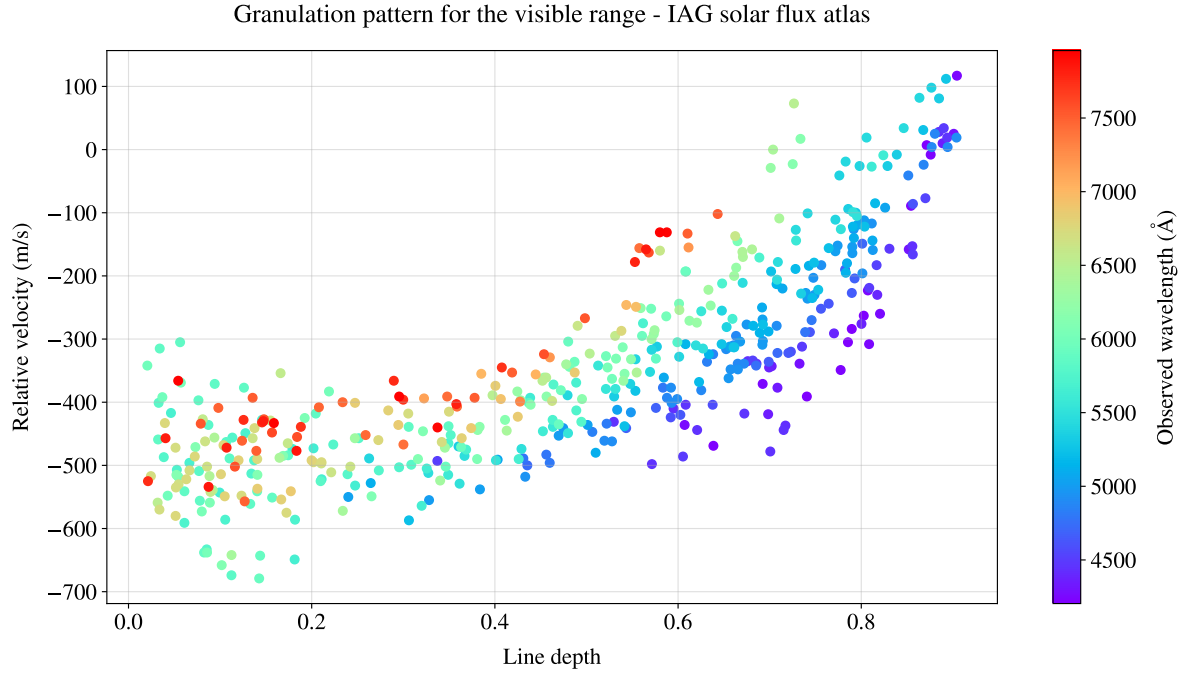
Figure 4.15: Granulation pattern obtained for both wavelength ranges in the IAG solar flux atlas. Note that the relative velocity is wavelength-dependent

As shown in Figure 4.15, the convective velocity depends on line depth, as described in literature. Moreover, this *granulation curve* is not unique or universal, but depends on the wavelength range. To further characterize this trend, we performed an analysis of line depth versus wavelength was performed at fixed velocities.

To measure these wavelength shifts, the analysis was restricted to the spectral range from 4300 Å to 5600 Å. One of the plots of Figure 4.16 illustrates why the restricted range is convenient: In longer wavelengths it presents more complex structures which make a linear fit useless. The wavelengths from both atlases were then sorted into velocity bins of 50 m/s.
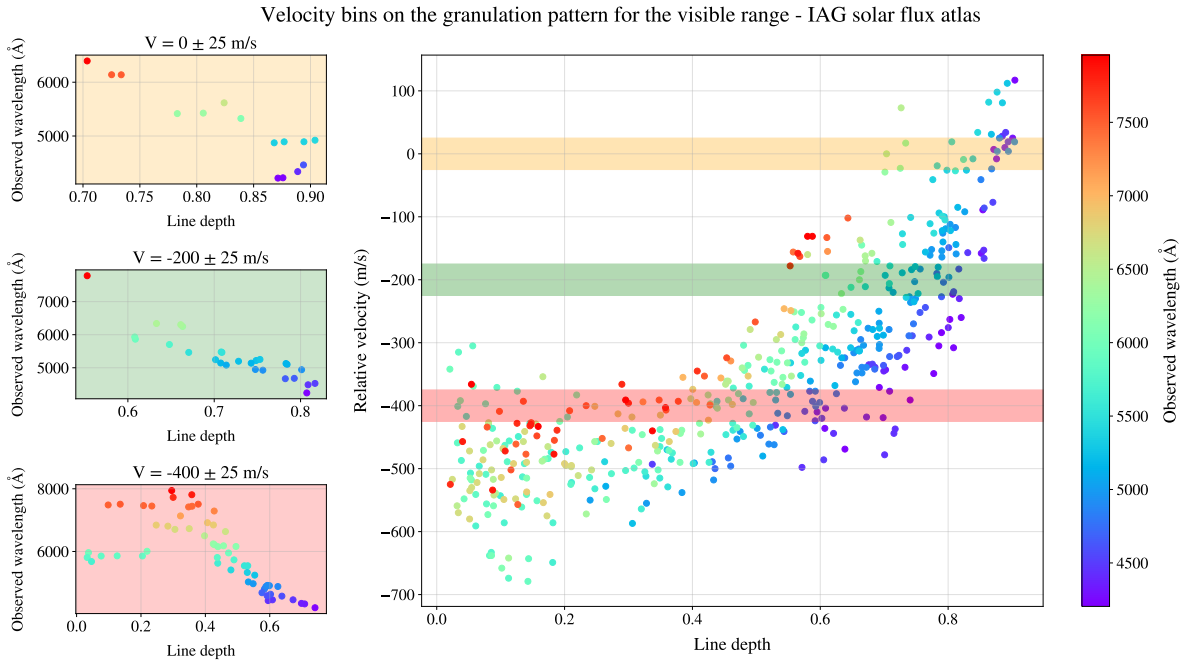
Figure 4.16: Velocity bins for the relation between wavelength and line depth.

For each velocity bin was plotted the wavelength against line depth to measure a frequency shift with a lineal fit (see Figure 4.17).
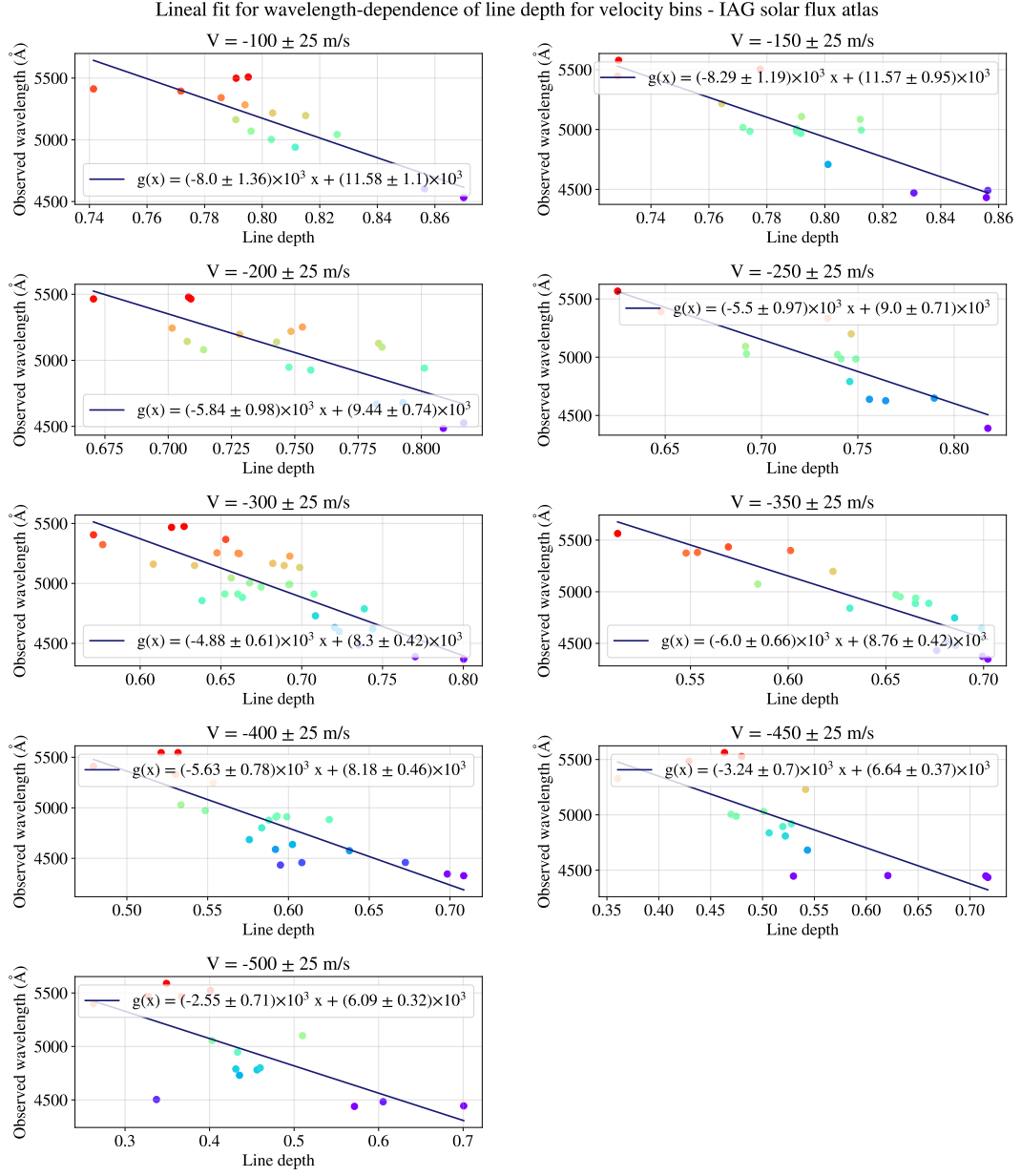
Figure 4.17: Individual plots of wavelength across line depth representing each bin of velocity for the IAG solar flux atlas.

The same analysis was performed to compare with the disk-center spectrum. The Figure 4.18 shows the results for the wavelength-dependence along line depth in the IAG spatially resolved quiet sun atlas.
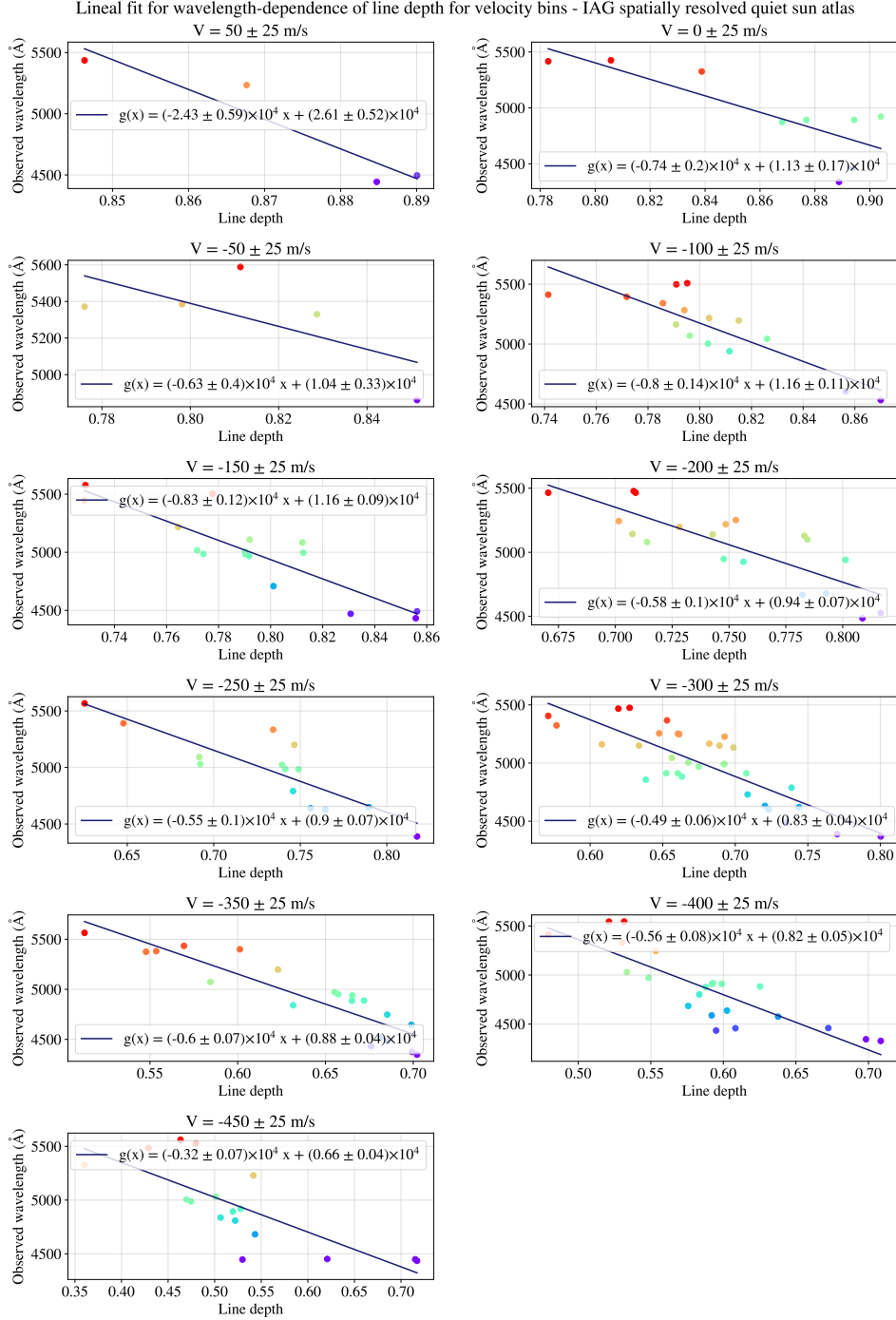
Figure 4.18: Individual plots of wavelength across line depth representing each bin of velocity for the IAG spatially resolved quiet sun atlas. The value for slopes on this spectrum are higher than the disk-integrated flux atlas.

IN PROGRESS The guiding hypothesis was: "If the velocity shift is present only in the disk-

integrated spectrum and absent at the disk-center, then solar rotation is the cause." However, the velocity shift was observed in both spectral datasets and the parameters on the disk-center spectrum are greater than IAG solar flux atlas. This was initially unexpected, as rotational doppler broadening is negligible at the disk center.

Furthermore, the shift on every lineal fit expresses the granulation relation. IN PROGRESS

4.3.2 Line depth-dependence on excitation potential for the lowest energy level

As shown Figure 4.19 the relative velocity was plotted against excitation potential for lowest energy level. The distribution of wavelength along excitation potential is according to literature, showing that lower wavelength have less excitation potential on the lowest energy level than high wavelength.
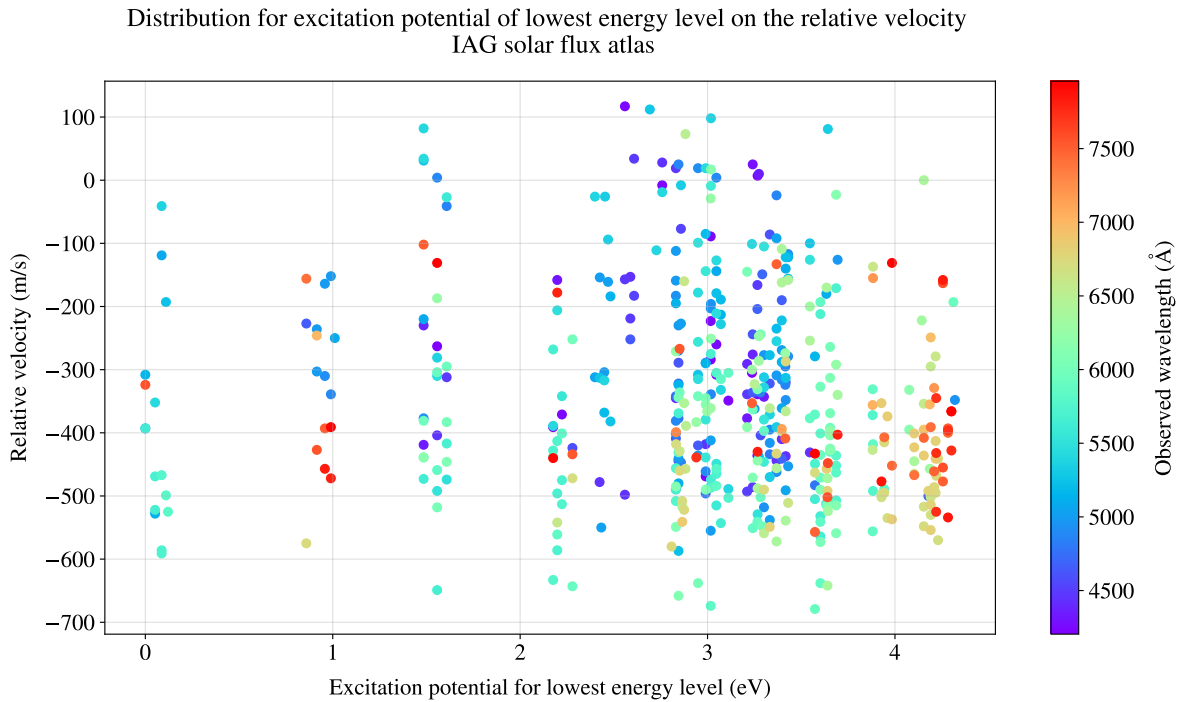
Figure 4.19: Relative velocity against excitation potential for lowest energy level in the visible range of the IAG solar flux atlas.

However, if relative velocity is separate on bins of 100 m/s and plot the excitation potential for

lowest energy level against line depth, shifts in the range (2.5 to 5.0) eV of excitation potential become apparent as shown Figure 4.20.
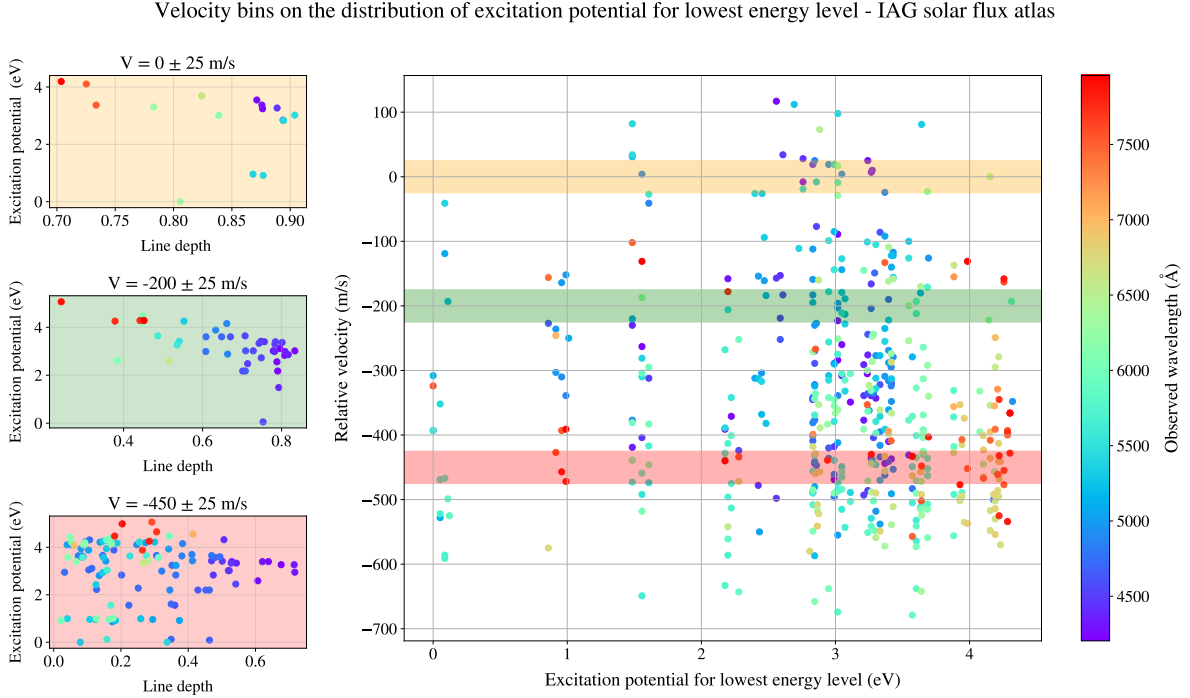
Figure 4.20: Velocity bins of 100 m/s across Figure 4.19, with this separation is visible the excitation potential shift in the range (2.5 to 5.0) eV across line depth.

Figure 4.21 explicitly shows the dependence on the highest values (2.5 to 5.0) eV for the excitation potential of lower energy levels across line depth, which can be modeled with a lineal fit.
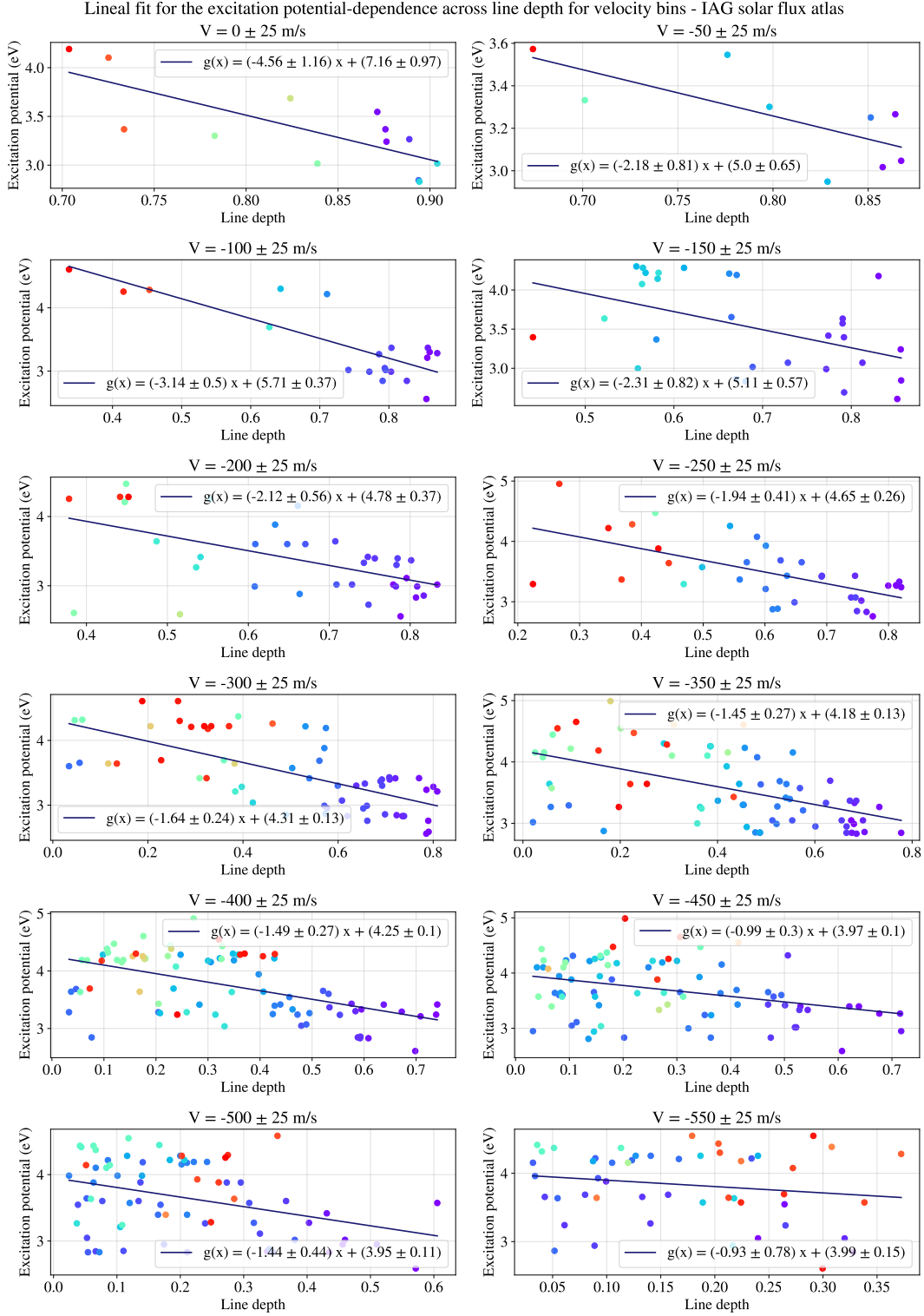
Figure 4.21: Individual plots for the range (2.5 to 5.0) eV of excitation potential of lower energy level across line depth, representing each bin of velocity for the visible range of IAG solar flux atlas. The Table 4.1 shows the coefficients for each applied lineal fit.

For the velocity range of -175 m/s to -525 m/s the calculated slopes are similar, as shown in Table 4.1. This indicates a consistent ratio on energy shifts in the energy across the velocity range.

Velocity bin (m/s)	Slop (eV)	σ_{Slope}	Shift (eV)	σ_{Shift}
0	-4.5638	1.1564	7.1636	0.9651
-50	-2.1781	0.8069	5.0005	0.6495
-100	-3.1355	0.4958	5.7114	0.3697
-150	-2.3102	0.8208	5.1098	0.5688
-200	-2.1203	0.5594	4.7782	0.3747
-250	-1.9361	0.4121	4.6533	0.2588
-300	-1.6399	0.2408	4.3146	0.1314
-350	-1.4534	0.2694	4.1778	0.1251
-400	-1.4863	0.2683	4.2510	0.1030
-450	-0.9916	0.2973	3.9734	0.0982
-500	-1.4429	0.4428	3.9506	0.1097
-550	-0.9308	0.7750	3.9919	0.1497

Table 4.1: Values for the lineal fit coefficients on the different velocity bins for the Figure 4.21. The values σ_{Slope} and σ_{Shift} refers to the standard error of the respective lineal coefficient.

To corroborate the only dependence on excitation potential of lowest energy level, the same analysis was performed on the IAG spatially resolved quiet sun atlas at $\mu = 0$.
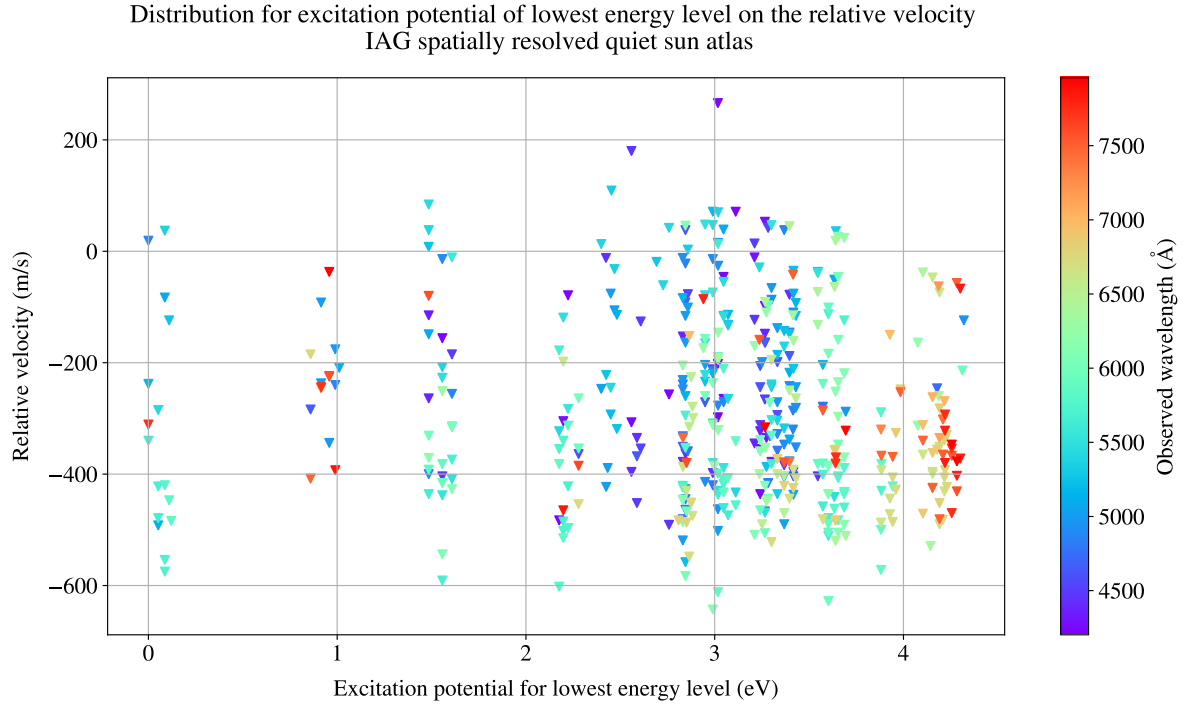
Figure 4.22: Relative velocity against excitation potential of lowest energy level in the visible range for the IAG spatially resolved quiet sun atlas.

Figure 4.22 shows the relative velocity against excitation potential of lowest energy level for disk center data.

Separating the relative velocity on bins of 100 m/s and taking the range (2.5 to 5.0) eV of excitation potential, the disk-center flux exhibits the same qualitative behavior as the IAG solar flux atlas (see Figure 4.23).
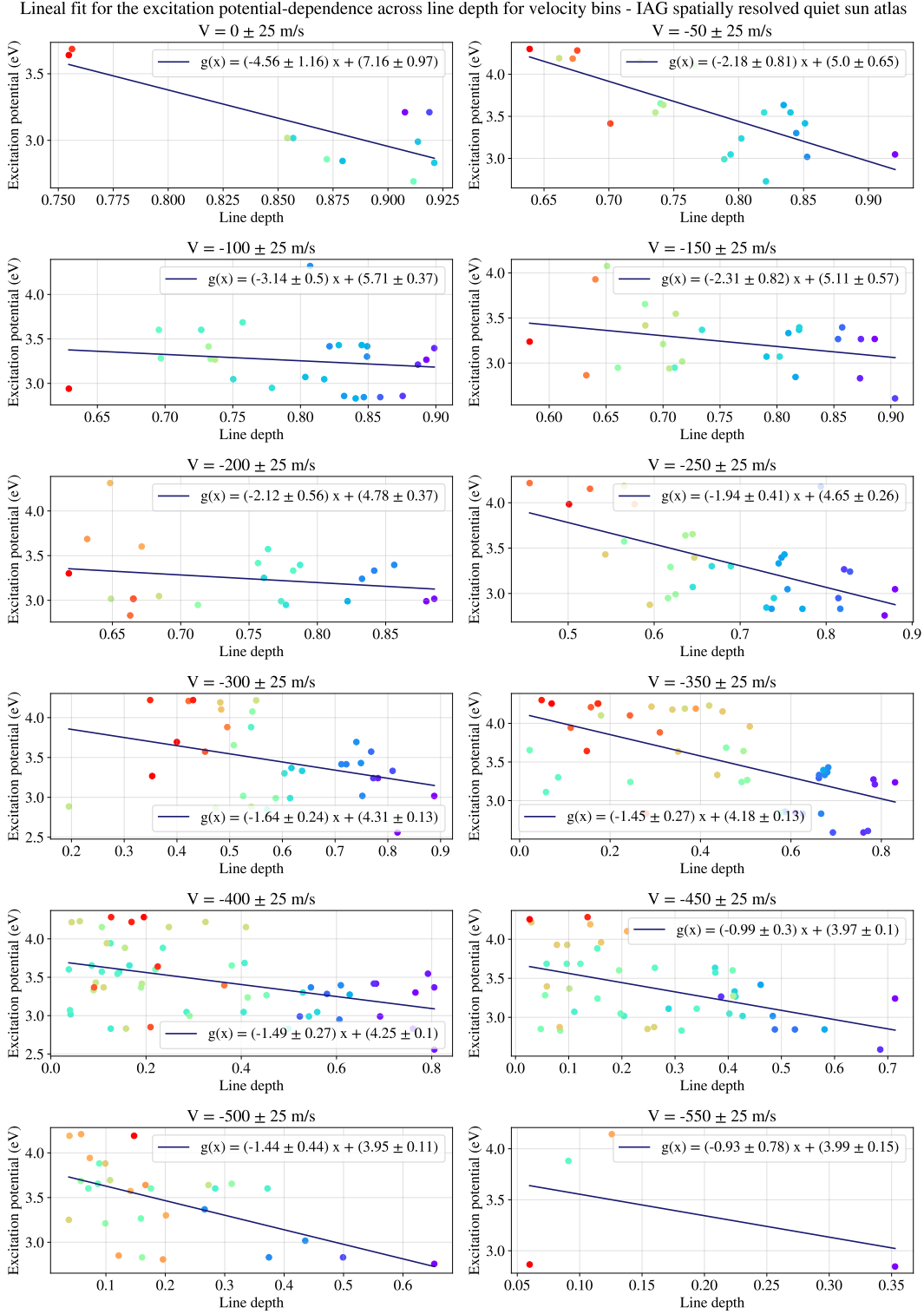
Figure 4.23: Individual plots for the range (2.5 to 5.0) eV of excitation potential of lowest energy level across line depth, representing each bin of velocity for the IAG spatially resolved quiet sun atlas.

However, there is a quantitative difference, the lineal fit coefficients are higher to the reported for the disk-integrated atlas (see Table 4.2).

| Velocity bin (m/s)	Slop (eV)	σ_{Slope}	Shift (eV)	σ_{Shift}
0	-4.5638	1.1564	7.1636	0.9651
-50	-1.9274	1.1583	4.7903	0.9496
-100	-2.9149	2.0695	5.5099	1.6744
-150	-2.7907	1.2421	5.4525	0.9195
-200	-2.8771	0.9840	5.3471	0.7277
-250	-2.1774	0.7516	4.8238	0.5241
-300	-0.9802	0.3714	3.8374	0.2419
-350	-0.3246	0.3473	3.4399	0.1931
-400	-0.9455	0.3184	3.8607	0.1511
-450	-0.7942	0.3032	3.7832	0.1174
-500	-1.1728	0.4614	3.7206	0.1291
-550	-1.8835	1.0826	3.9324	0.1770

Table 4.2: Values for the lineal fit coefficients on the different velocity bins for the Figure 4.23. The values σ_{Slope} and σ_{Shift} refers to the standard error of the respective lineal coefficient.

IN PROGRESS.. The rotation eliminates one of the chromodependence but this dont confirm anything IN PROGRESS..

4.3.3   Characterization of chromodepence on granulation pattern

The Figure 4.24 show the standard curve proposed for Gray and Oostra [8], establish on the range $6020\,\text{Å} - 6340\,\text{Å}$ of wavelength.
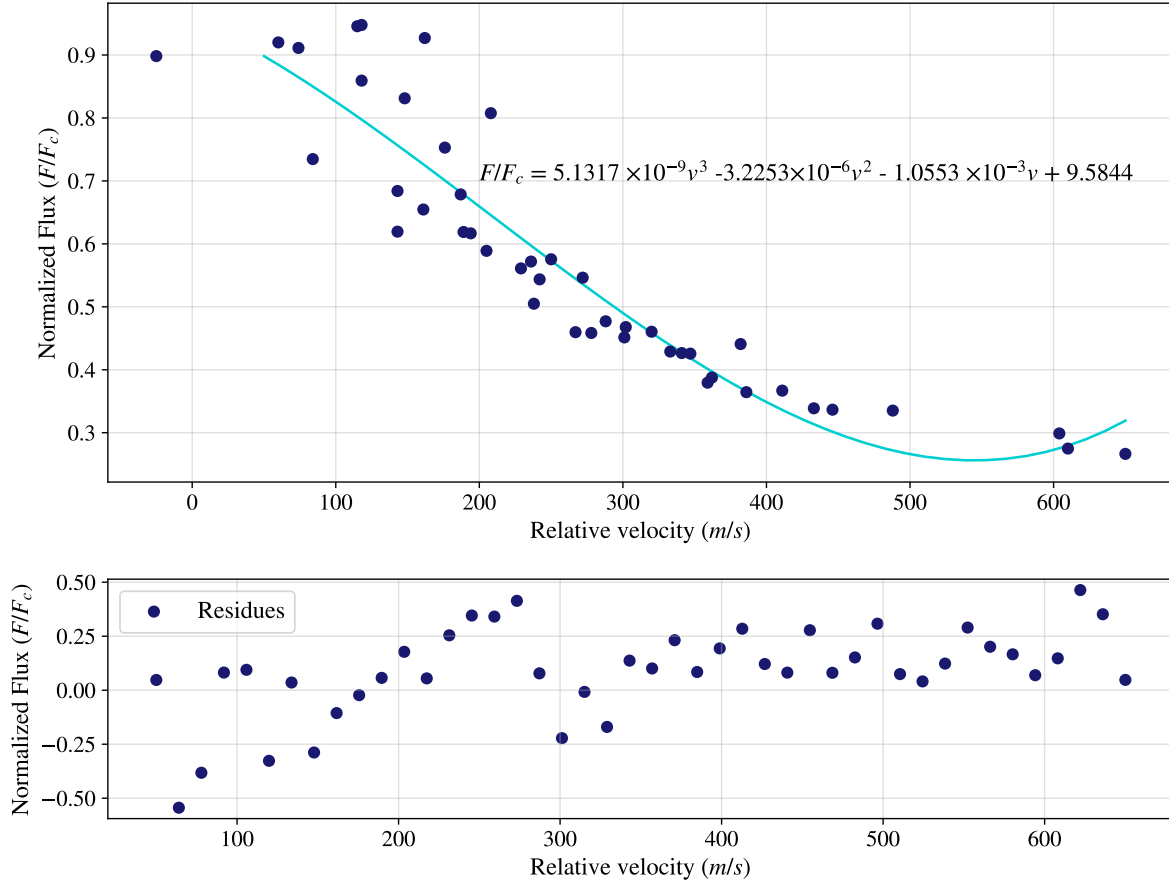
Figure 4.24: Standard curve given by Gray and Oostra and recalculated for comparision with the current work.

Since the standard curve does not account for the full wavelength range and the given third-order polynomial fit take just the low curve points, a different approach was adopted. The spectrum was separated into distinct color ranges, and a second-order polynomial was adjusted to each segment as shown Figure 4.25.

Figure 4.25: Different color curves adjusted to a specific range on granulation pattern for the visible range in the IAG solar flux atlas. The inclination on the curves is more pronounced in the violet than the red range.

The trend in the curves is more pronounced in the violet and red ranges. This can be interpreted as a shift and flattening of the standard curve from Gray and Oostra towards shorter wavelengths. Using the curve for the range $(4970\,\text{Å} - 5700\,\text{Å})$ as a reference (green color curve), distinct scaling coefficients were calculated for each color segment, as shown in Table 4.3.

Wavelength range ($\mathring{A}$)	Color coefficient
3800-4270	0.5359
4270-4760	0.8195
4760-4970	0.8348
4970-5700	1.000
5700-5810	1.0595
5810-6180	0.9834
6180-7800	1.1149

Table 4.3: Scaling factors α_c to the new standard curve shown in the Equation (4.1).

The Equation (4.1) reports a new, color dependent standard curve. Its coefficients (α_c) vary with the color range, generating the corresponding granulation pattern for each spectral segment listed in Table 4.3.

$$F/F_c = \alpha_c(1.2925 \times 10^{-6}v^2 - 0.0019v + 0.8671) \tag{4.1}$$

However, when the color coefficients α_c are plotted against wavelength, they exhibit a quadratic tendency that increases with longer wavelengths. This finding leads us to model the coefficient α_c as a function of wavelength, as shown in equation (4.2)

$$\circledast(\lambda) = -6.7598 \times 10^{-8}\lambda^2 + 9.1584 \times 10^{-4}\lambda - 2.0041 \tag{4.2}$$

Then, the characterization for the granulation pattern it can be described by equation 4.3

$$F/F_c(\lambda, v) = \circledast(\lambda)[1.2925 \times 10^{-6}v^2 - 0.0019v + 0.8671] \tag{4.3}$$

On the other hand, chromodependence was also identified in the near infrared range, although it is less pronounced than in the visible spectrum. There were defined specific wavelength ranges by excluding regions dominated by telluric absorption lines, and was found linear relationships for each range (see Figure 4.26). However, unlike the visible range these relationships do not exhibit a unified correlation.
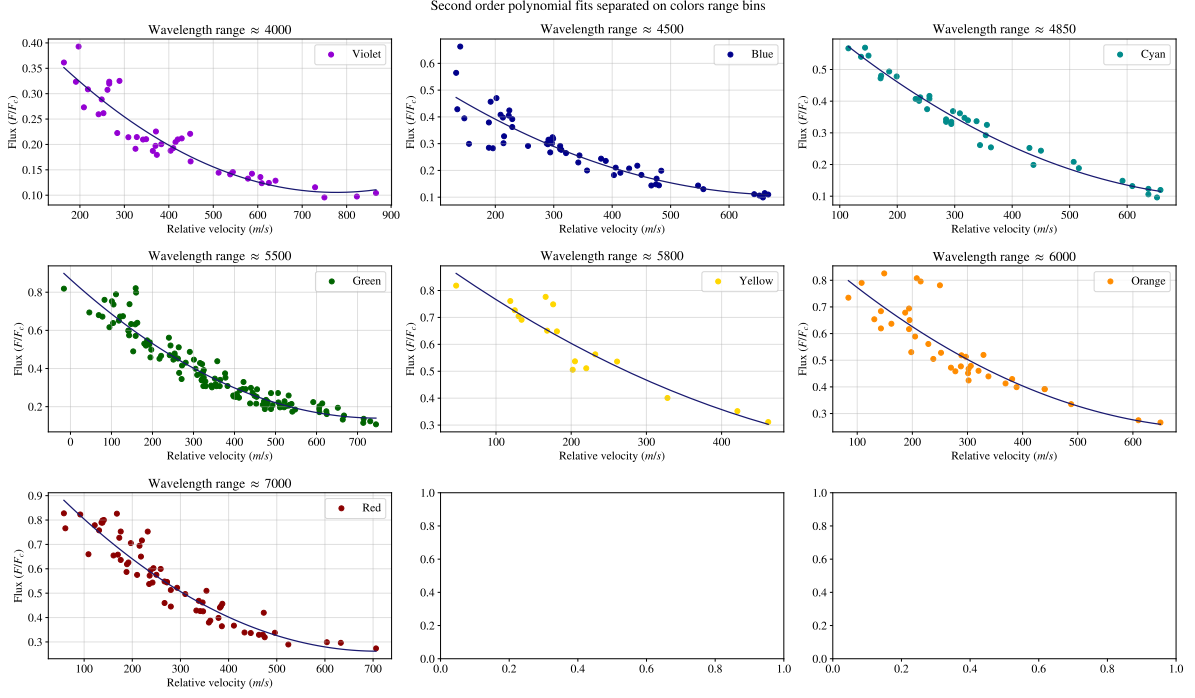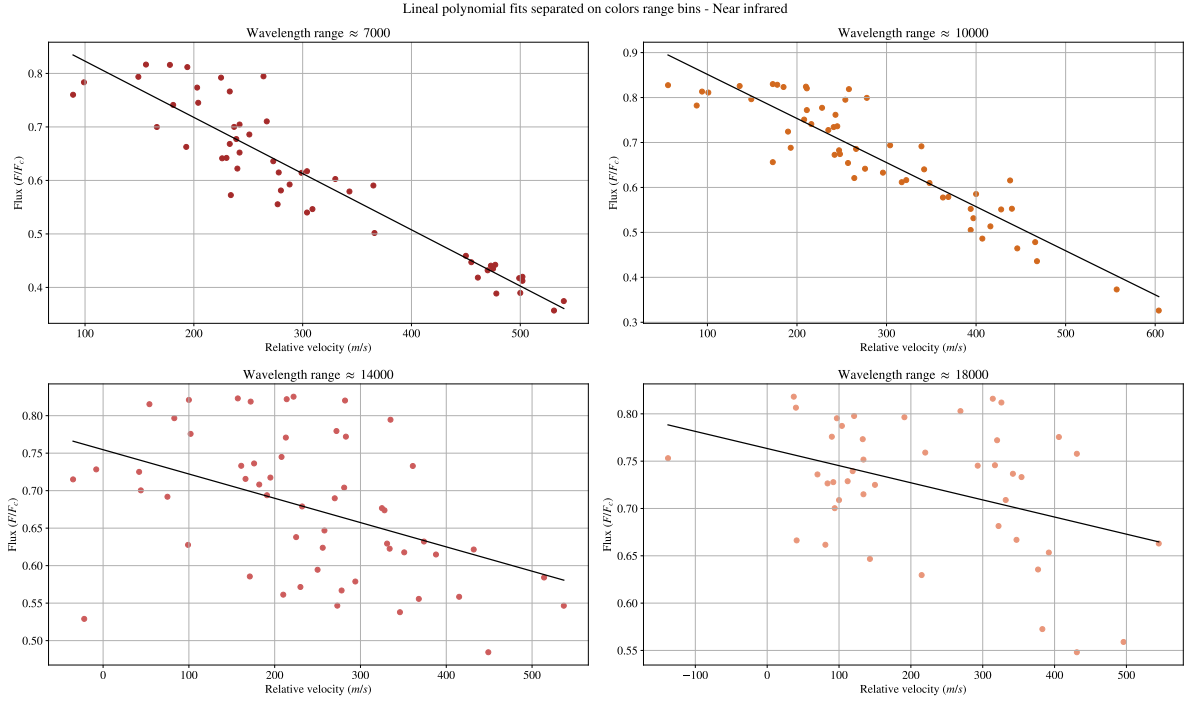
Figure 4.26: Different color curves fitted to a specific ranges on granulation pattern for the near infrared range in the Solar Flux Atlas.

The coefficients for each linear fit applied are shown in the table 4.4.

Wavelength range	Slope	Shift
7000-8500	-0.0010	0.9279
8500-11000	-0.0009	0.9496
11000-16000	-0.0003	0.7546
16000-23000	-0.0001	0.7633

Table 4.4: Coefficients for the first order polynomial fit in each wavelength range in the near infrared.

4.4 Higher quality graphs

To show the improvement on the quality in the third signature plots, the figure 4.27 compare the plot obtained by Ellwarth [7] and the granulation pattern obtained in this project.
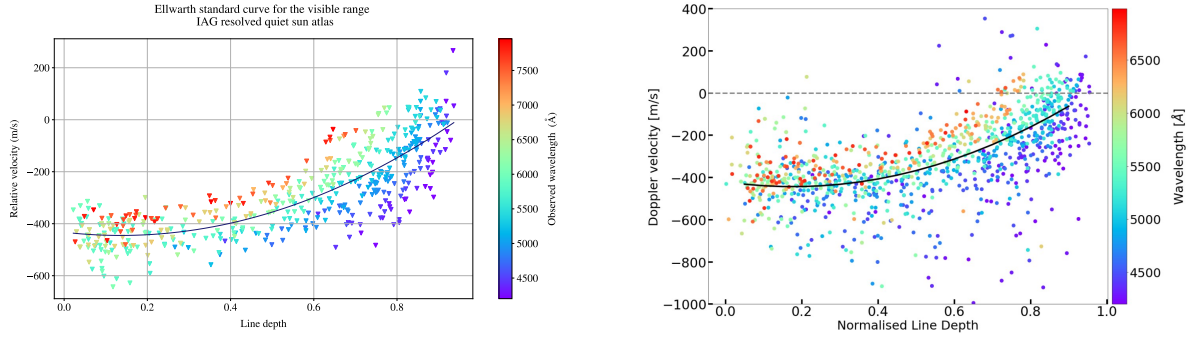
Figure 4.27: We realized the same graphic for the comparision with the Ellwarth article to show the less scattered points.

The less scattered points and the improvement on the chromodepence identification is evident. IN PROGRESS Discuss all aspects about the standard granulation curve and the effects that broaden or disperse this curve: The curve depends strongly on wavelength and weakly on excitation potential. Discuss the hypothesis that the chromodependence is a consequence of rotation and why now believe that is not true. IN PROGRESS

Chapter 5

Conclusions

In conclusion, this project characterized the convective blueshift in solar absorption lines and its dependence on both line depth and wavelength range.

Specifically, was produced a refined, blend-free list of Fe I lines and derived solar granulation patterns with minimal scatter. Also provided a detailed description of how the granulation pattern varies with wavelength, establishing a new, color-dependent standard curve.

(In progress..)

Appendix A

Z-score Standardization

The function np.polyfit (), during the process of calculating the fourth-order polynomial fit, presents an over estimation on the coefficients due to the large difference of magnitude order between axes. To deal with this difference, was applied a z-score standardization on the selected bins of wavelengths around the minimum reference point. This process helps to avoid the dominance of certain features over others due to differences in their scales [19].

For the standardization was applied Equation (A.1) on the selected bins for wavelength around the minimum reference point.

$$\lambda_{\text{scaled}} = \frac{\lambda_{\text{original}} - \mu(\lambda_{\text{original}})}{\sigma(\lambda_{\text{original}})} \tag{A.1}$$

Where $\mu(\lambda_{\text{original}})$ refers to the mean and $\sigma(\lambda_{\text{original}})$ to the standard deviation of the wavelength range. In terms of calculating derivatives for the first and second signature of convection, the standarization on the variable required a re-scaled factor of conversion for obtain the original values. Based on the definition for the standardization, the derivatives have to follow Equation (A.2).

$$\frac{d}{d\lambda_{\text{original}}} = \frac{1}{\sigma(\lambda_{\text{original}})} \frac{d}{d\lambda_{\text{scaled}}} \tag{A.2}$$

Taking the derivative of the expression (A.1) a factor related to the standard deviation appears. Therefore, the original values for derivatives evaluated in the observed wavelength are expressed in Equation (A.3)

$$\frac{d^2}{d\lambda_{\text{original}}^2} = \frac{1}{\sigma(\lambda_{\text{original}})^2} \frac{d^2}{d\lambda_{\text{scaled}}^2} \qquad \frac{d^3}{d\lambda_{\text{original}}^3} = \frac{1}{\sigma(\lambda_{\text{original}})^3} \frac{d^3}{d\lambda_{\text{scaled}}^3} \qquad (A.3)$$

The treatment proposed solves the problem for the large difference of magnitude order between axes.

Appendix B

The third derivate relation

The third derivate relation or called the line profile bisector slope was deducted by Professor Benjamin and showed below.

Defined the slope as equation (B.1), where the points b, c, h are illustrated in the figure **??**

$$CBS = \lim_{h \to 0} \frac{\frac{b+c}{2} - a}{h} \tag{B.1}$$

Note that in a symmetrical line the bisector is vertical and the slope, according to this definition, is zero. Now, the curve may be expanded around the point a by Taylor series noticing that a is chosen at the minimum, so $f'(a) = 0$ and $f(c) - f(a) = h$,giving

$$2h = (c - a)^2 f''(a) + \frac{1}{3}(c - a)^3 f'''(a) \tag{B.2}$$

We may abbreviate $c - a = x > 0$ and likewise $b - a = y < 0$ obtaining

$$2h = x^2 f''(a) + \frac{1}{3}x^3 f'''(a) \qquad 2h = y^2 f''(a) + \frac{1}{3}y^3 f'''(a) \tag{B.3}$$

So, x and y are two equations roots. One of the possible roots for the cubic polynomial equation, the two that are needed whose that trend to

$$CBS = \lim_{h \to 0} \frac{x}{y} = -1 \tag{B.4}$$

If the polynomial equation is written in the standard form $ax^3 + bx^2 + cx + d = 0$ the coefficients

are $a = \frac{f'''}{3}$, $b = f''$, $c = 0$, $d = -2h$. A standard procedure is to change the variable to $x = t - \frac{b}{3a} = t - \frac{f''}{f'''}$ which produces the "depressed" equation.

$$t^3 + pt + q = 0 \quad \rightarrow \quad p = -3\left(\frac{f''}{f'''}\right)^2 \quad q = 2\frac{(f'')^3 - 3h(f''')^2}{(f''')^3} \tag{B.5}$$

Where the equation have three solutions of the form:

$$t_i = 2\left(\frac{f''}{f'''}\right)\cos\left(\frac{1}{3}\arccos\left(\frac{3h(f''')^2}{(f'')^3} - 1\right) - \frac{2\pi i}{3}\right) \tag{B.6}$$

When h vanishes, there are two equal solutions and one differing. Let's abbreviate

$$\epsilon = \frac{h(f''')^2}{(f'')^3} << 1 \tag{B.7}$$

In the limit $h \rightarrow 0$ we have $\epsilon << 1$ which means $\arccos(3\epsilon - 1) = \pi - \delta$ with δ an small angle. So, $\delta = \sqrt{6\epsilon}$ and the solution is the next equation.

$$t_{\pm} = 2\frac{f''}{f'''}\left(\frac{1}{2}\cos\left(\frac{\sqrt{6\epsilon}}{3}\right) - / + \frac{\sqrt{3}}{2}\sin\left(\frac{\sqrt{6\epsilon}}{3}\right)\right) \tag{B.8}$$

For the bisector slope appears the next condition.

$$x + y = t_+ + t_- - 2\left(\frac{f''}{f'''}\right) = -\frac{2}{3}\left(\frac{f''}{f'''}\right)\epsilon = -2h\frac{f''}{3(f''')^2} \tag{B.9}$$

Whence, finally, the core bisector slope is defined by equation (B.10)

$$CBS = -\frac{f''}{3(f''')^2} \tag{B.10}$$

In the code it was multiplied by the relation $(\frac{c}{\lambda})$ to see the behavior across line depth in the graphic.

Appendix C

Visualizer for outliers

For the line selection process mentioned in Chapter 3, a visualizer was created using the Tkinter library to aid in identifying blend lines or those outside the spectrum.

Two versions of the visualizer were developed, each utilizing different filters. The first filter displays the geometry of the line core and the line profile c-curved bisector. The second filter, which builds on the selected lines from the first, shows the three signatures of convection and the behavior of the selected line in each one.

This visualizer significantly reduced the time spent reviewing lines. It also features a custom classification system, shown as color stars. These buttons don't make something on the Dataframe more than just a label for the user orientation. Also, allows the users to add lines to a DataFrame, specially for the lines which are gonna to be deleted or filtered due to bad reputation, and save images. The code for the visualizer can be seen on GitHub, along with a test example provided below.

The main code for this project is contained in the file Visualizer.ipynb, and a test example dataset is provided in test.xlsx. To facilitate analysis, two DataFrames were created: One for the spectrum with columns Wave and Flux, representing wavelength in Armstrongs and normalized flux, respectively, and another for the list of Fe I lines. The closer lines function was used to select the closest minimums to the Fe I lines, along with their associated flux values and Fe I line wavelengths.

Beware, these Fe I line wavelengths serve as reference points for selecting bins around each

line, rather than representing observed wavelengths. The function discards any lines with distances between minimums and Fe I lines exceeding $0.001\mathring{A}$. Furthermore, to ensure convexity, fourth-order polynomial fits with non-positive second-order coefficients were discarded. An approximation was used to discard lines that do not belong to the spectrum.

A computational form of a slope can be seen as the difference between the maximum and minimum point of the list of points. In terms of flux if it is seen the distance can't be more than a half of the absolute difference. This lets us discard pronounced slopes without affecting or filtering weaker lines. Then use the function local points for selecting the bins of $0.1m\mathring{A}$ around the minimal point, each corresponding to one index on the closer lines dataframe.

The function Fit Derivatives finds the fourth order polynomial fit and calculates the minimum point with the second derivative of the fit, that is the observed wavelength. This returns a Dataframe with the value of Fe I line associated, the polynomial fit, and the observed wavelength. In parallel, the line profile bisector is calculated using the midpoint method where equal points of flux are selected for comparison.

The first visualizer uses these calculated values, showing the line core and the fourth polynomial fit, in parallel with the line profile bisector of each one in terms of velocity.

We recommend eliminating the lines that follow one of the conditions presented. First, the line profile bisector doesn't show a C-curved bisector or it's too affected by the noise. Second, the polynomial fit and the line profile don't follow a common absorption line form. This can be interpreted as the position on other points to the fit. Third, the line core shows two minimums or a protuberance. These are blended lines. An example of this behavior is shown on figure (). The objective of the first filter is to reduce the number of lines for analyzing the three signatures of convection.

The second part of the code calculates the three signatures of convection for the filtered lines. The second visualizer shows all the graphics including the line profile with the polynomial fit. In each graphic of derivatives the corresponding Fe I is resalted, this with the finally to select lines depending on his behavior.

C.1 Test example

In the file test example.ipynb run the line code.

```
raw_data = read.csv(jsjsjsj)
```

Feel free to modify this line to read the file type. The idea is the Dataframe results have the columns Wave (cm), nFlux and Wave A. There's no need for the flux to be normalized, because nothing in the code uses the condition of normalized flux. Then run the list of calibration lines. In this case, we use the Nave list of Fe I lines. A test example list is displayed on the carpet Data.

```
raw lambda =
```

Run the next two cells where the functions closer lines and local points are displayed.

```
closer_lines_first_filter =
local_points_first_filter=
```

With this dataset, run the cell for the applied the first filter.

```
Values_first_filter, Local_first_filter, Fit_first_filter,
   Bisector_first_filter = First_Filter()
```

On the cell code for the visualizer just comment the cell before running.

```
app1= app(run, local_first_filter)
```

To extract the Dataframe with the lines to drop or for further analysis run the cell. Make sure that the visualizer is closed after running another cell code.

```
Dataframe to drop =
```

The cell saves the filtered lines and the suspect ones in two different xlsx files.

```
Values.save()
```

With the new list of filtered lines, run the cell to redefine the list of Fe I lines with only the filtered ones.

```
raw lambda =
```

Now, run again the code for closer lines and local points with the new list of Fe I lines. Then run the cell for applied the second filter and calculate the three signatures of convection

```
Values_second filter = Second Filter ()
```

As the same with the first filter, just comment the line to observe the second filter.

```
app2= Second filter (run, local points, values)
```

The cell helps to extract the lines to drop and remove it for the Dataframe.

```
Values.save ()
```

After the process, the resulting excel is the definitive list of Fe I lines.

Bibliography

[1] Priest Eric. *Solar magnetohydrodynamics*. Kluwer, 1982.

[2] Jean-Marie Malherbe. Jules janssen, the birth of solar physics, the foundation of meudon observatory and the mont blanc adventure (1875-1895). *HAL CNRS*, August 2022.

[3] Samir A Hamouda, Faten F Alfarjani, and Fathi Y Elfituri. Sunspots production and relation to other phenomena: A review. *International Journal of Science and Research Methodology*, 06 2018.

[4] Foukal Peter. *Solar Astrophysics*. Cambridge research and instrumentation, 1990.

[5] D. Dravins, L. Lindegren, and A. Nordlund. Solar granulation - influence of convection on spectral line asymmetries and wavelength shifts. *Astronomy and Astrophysics*, 96:345–364, March 1981.

[6] Timo A. Nieminen. Solar line asymmetries: Modelling the effect of granulation on the solar spectrum. *arXiv*, August 2017. arXiv:1708.06408 [astro-ph].

[7] M. Ellwarth, B. Ehmann, S. Schäfer, and A. Reiners. Convective characteristics of fe i lines across the solar disc. *Astronomy and Astrophysics*, 680:A62, December 2023.

[8] David F. Gray and Benjamin Oostra. The solar-flux third granulation signature. *The Astrophysical Journal*, 852:42, January 2018.

[9] David F. Gray. The third signature of stellar granulation. *The Astrophysical Journal*, 697(2):1032, May 2009.

[10] Devon Hamilton and John B. Lester. A technique for the study of stellar convection: The visible solar flux spectrum. *Publications of the Astronomical Society of the Pacific*, 111(763):1132, September 1999.

[11] David F. Gray and Teznie Pugh. The third signature of granulation in bright-giant and supergiant stars. *The Astronomical Journal*, 143(4):92, March 2012.

[12] Benjamin Oostra and Paula Catalina Vargas Muñoz. The differential redshift of titanium lines in k stars. *Revista mexicana de astronomía y astrofísica*, 58(2):173–180, 2022.

[13] A. Reiners, N. Mrotzek, U. Lemke, J. Hinrichs, and K. Reinsch. The iag solar flux atlas: Accurate wavelengths and absolute convective blueshift in standard solar spectra. *Astronomy and Astrophysics*, 587:A65, March 2016.

[14] H. H. Plaskett. Solar granulation. *Monthly Notices of the Royal Astronomical Society*, 96:402, March 1936.

[15] B.W. Carroll and D.A. Ostlie. *An Introduction to Modern Astrophysics*. Cambridge University Press, 2017.

[16] G. Nave, S. Johansson, R. C. M. Learner, A. P. Thorne, and J. W. Brault. A new multiplet table for fe i. *The Astrophysical Journal Supplement Series*, 94:221, September 1994.

[17] C. Allende Prieto and R. J. Garcia Lopez. Fe i line shifts in the optical spectrum of the sun. *Astronomy and Astrophysics Supplement Series*, 129:41–44, April 1998.

[18] I.S. McLean. *Electronic Imaging in Astronomy: Detectors and Instrumentation*. Springer Praxis Books. Springer Berlin Heidelberg, 2008.

[19] John P. Boyd. *Solving Transcendental Equations: The Chebyshev Polynomial Proxy and Other Numerical Rootfinders, Perturbation Series, and Oracles*. SIAM, October 2014.

[20] Juan Sebastian Aponte. *Medición de la velocidad convectiva en la fotosfera solar*. Bachelor's thesis, Universidad de los Andes, 2017.

[21] David F. Gray. Empirical decoding of the shapes of spectral-line bisectors. *The Astrophysical Journal*, 710(2):1003, January 2010.

[22] David F. Gray and Kevin I. T. Brown. Precise spectroscopic radial velocity measurements using telluric lines. *Publications of the Astronomical Society of the Pacific*, 118(841):399, March 2006.

[23] David F. Gray. *The Observation and Analysis of Stellar Photospheres*. Cambridge University Press, 3 edition, 2005.

[24] F. Stief, J. Löhner-Böttcher, W. Schmidt, T. Steinmetz, and R. Holzwarth. Convective blueshifts in the solar atmosphere - ii. high-accuracy observations of the fe i 6173.3 Å line and deviations of full-disk dopplergrams. *Astronomy and Astrophysics*, 622:A34, February 2019.

[25] Barbara Ryden. *Introduction to cosmology*. Cambridge University Press, 2016.

[26] Alessandro Cacciani, Runa Briguglio, Fabrizio Massa, and Paolo Rapex. Precise measurement of the solar gravitational red shift. *Celestial Mechanics and Dynamical Astronomy*, 95:425–437, May 2006.